

POLITECNICO DI TORINO

Master's Degree in Electronic Engineering



Master's Degree Thesis

Extraction of Peronospora infection through the analysis of hyperspectral data

Supervisor:
Prof. Andrea Maria LINGUA

Candidate:
Francesca SPANNA

Academic Year 2020-2021

"Nec minor est virtus quam quaerere parta tueri"
(Ovidio, *Ars amatoria*, II, v.13)

Abstract

In the last years, a great interest in precision agriculture field has developed. Technology strongly supports this strategy employing innovative concepts and tools to assist farmers in agricultural processes management. Sensors, typically mounted on UAVs (Unmanned Aerial Vehicles) or UGVs (Unmanned Ground Vehicles), play a fundamental role in the described scenario since they allow an extensive evaluation of the framed object with a high detail level.

In this context, the present thesis aims to analyze the data gathered through the hyperspectral camera Rikola in an Astigian vineyard. The acquired images show vine leaves affected by a typical vine disease, Peronospora, caused by a fungus, *Plasmopara viticola*. The effect is the generation of spots on the leaves with the consequent leaves necrosis, but damages can extend to branches and grapes. This represents a loss of resources and therefore a reduction of production. For these reasons, it is important to prevent or at least limit the expansion of Peronospora in vineyards. Thanks to the continuous technological development, plants health control and autonomous identification of several phenomena are becoming key operations. This thesis work is propaedeutic to the explained goals: an initial calibration phase is applied in order to remove the influence of external factors on acquired data. Then calibrated images are elaborated with machine learning algorithms to perform a classification process, which leads to obtain a classifier able to identify Peronospora effects on vine leaves and that can be employed in different applications.

Acknowledgments

This thesis work represents the conclusion of a difficult but not emotionless path. It has been developed with the collaboration of PIC4SeR, Interdepartmental Center for Service Robotics at Politecnico di Torino.

I would like to extend my sincere thanks to Prof. Andrea Maria Lingua, who guided and assisted me throughout this study giving me the possibility to explore new and interesting themes.

I am grateful to my family, always present and willing to support and encourage me in every situation.

A special thought is dedicated to all my friends that shared every moment and contributed to make these years wonderful.

Table of contents

Abstract	I
Acknowledgments	II
List of tables	V
List of figures	VI
1 Introduction	1
2 Materials and Methods	4
2.1 Remote Sensing	4
2.1.1 Sensors	6
2.1.2 Hyperspectral camera Rikola	9
2.2 Peronospora	12
2.3 Mapir	14
3 Geometric Calibration	16
3.1 Camera Parameters	16
3.1.1 Intrinsic parameters	18
3.1.2 Extrinsic parameters	20
3.1.3 Distortion coefficients	20
3.2 Image aquisition	23
3.3 Procedure	24
3.3.1 Bands separation	25
3.3.2 Camera parameters estimation	25

3.3.3	Camera parameters elaboration	26
3.3.4	Bands calibration	31
3.3.5	Bands combination	32
4	Radiometric Calibration	33
4.1	Digital Numbers, Reflectance	33
4.2	Procedure	35
4.2.1	Datasets identification	39
4.2.2	Calibration relation definition	42
4.2.3	Calibration	46
4.3	Comparison among images results	48
5	Classification	51
5.1	Procedure	52
5.1.1	Training and Classification	53
5.1.2	Accuracy estimation	59
5.2	Porting	65
5.3	Application	69
6	Conclusions	71
	Bibliography	73

List of tables

3.1	<i>Acquisitions settings</i>	23
3.2	<i>Averaged intrinsic parameters: on the left top intrinsic matrix of Sensor 1 is reported, on right top intrinsic matrix of Sensor 2, on the bottom table with distortion coefficients for both Sensors. All the values are averaged quantities.</i>	31
5.1	<i>Classes color code: this table indicates the classes selected in this study, the color code associated to them and the identifier used in ArcGIS Pro.</i>	53
5.2	<i>First group of settings selected to perform classification.</i>	57
5.3	<i>Second group of settings selected to perform classification.</i>	58
5.4	<i>Accuracy measurements: these tables report the accuracy measurements for all the tested cases on image 'Peronospora_2.bsq': SVM-500, RT-30,50,1000, SVM-0 and RT-30,500,0. For each of them, training and verification ROIs are employed to estimate the accuracy.</i>	63
5.5	<i>Porting accuracy: these tables report the accuracy measurements obtained after the Porting application on the image 'Peronospora_3': the same methods and their configuration tested in the previous section are used, SVM-500, RT-30,50,1000, SVM-0 and RT-30,500,0.</i>	66

List of figures

2.1	<i>Electromagnetic spectrum: representation of the bands ranges. Energy increases with frequency, inversely to the wavelength. [1]</i>	5
2.2	<i>Active vs passive sensors: on the left a representation of an active device is reported, which detects the reflected radiation that has been emitted by itself. On the right, an example of a passive sensor that exploits sunlight is represented. [2]</i>	6
2.3	<i>Acquisition modes: in the drawings, x and y are the spatial coordinates of the pixels, while λ is referred to the wavelength axis. Figure A corresponds to a BIP mode, Figure B to a BIL technique, Figure C represents BSQ and Figure D corresponds to SS [3]</i>	9
2.4	<i>Rikola hyperspectral camera from DIATI at Politecnico di Torino</i>	9
2.5	<i>Fabry Perot interferometer: in the cavity formed by the two plates several reflections occur and only specific components are transmitted out of it.</i>	10
2.6	<i>Fabry Perot interferometer modes: only specific wavelengths can be transmitted. The selected ones depends on the cavity length. [4]</i>	11
2.7	<i>Representation of the Plasmopara viticola life cycle: after the primary infection, other multiple secondary infections can occur. Then the survival stage during winter. [5]</i>	12
2.8	<i>Representation of Peronospora effects on vine leaves: on the left oil spots in the upper side are shown, on the right oil spots in the lower side [6].</i>	13
2.9	<i>Mapir panel: target object with reference values [7]</i>	15

3.1	<i>Extrinsics and intrinsics trasformation: from 3D to 2D. External parameters connect the 3D coordinates of the real world and the camera. The transformation in the 2D dimension is performed by the intrinsic parameters.</i>	17
3.2	<i>Transformation of the real object in an image. Relation between object space and image space [8]</i>	18
3.3	<i>Skew representation: the blue drawing represents the original pixel matrix, where x and y axis are perfectly perpendicular. The red rectangle shows the effect of the skew parameter, since the two axes are not orthogonal.</i>	19
3.4	<i>Extrinsics: rotation and traslation are applied passing to the camera coordinate system. [9]</i>	20
3.5	<i>Effect of radial distortion: on the left the image not affected by distortion is represented; the center figure shows the barrel effect that characterizes the image; on the right pinchusion effect affecting the image is shown. [10]</i>	21
3.6	<i>Radial distortion behavior: on the left a typical barrel behavior is presented, characterized by negative values of the distortion parameter; on the right the pincushion behavior with radial distance is shown, characterized by positive values of the radial distortion [11]</i>	21
3.7	<i>Tangential distortion is caused by a missed alignment of the sensor with respect to the lens [12]</i>	22
3.8	<i>Radial and tangential distortion effect: the observed point does nort correspond to the predicted one. [13]</i>	22
3.9	<i>Checkerboard panel: it is the object of the acquisitions. [14]</i>	24
3.10	<i>Extrinsics: on the left camera-centric view is shown, hence all the panel positions with respect to the camera appear. On the right pattern-centric configuration is represented: it corresponds to the performed case.</i>	26
3.11	<i>Focal length vs wavelength: two distinct groups are visible. The blue points are referred to Sensor 1, the green ones to Sensor 2</i>	27

3.12	<i>Principal point vs wavelength: two groups can be identified. The blue ones characterize the Sensor 1 and are more spread around the average value, while the green set is referred to the Sensor 2 and appear more compact.</i>	28
3.13	<i>Skew vs wavelength: blue points belong to Sensor 1, green points to Sensor 2. No great differences between the two groups are visible. . . .</i>	29
3.14	<i>Radial distortion vs pixel distance: a behavior typical of barrel effect is visible. As the pixel is near to the edge (i.e. pixel distance increases), the distortion is more visible. Sensor 1 presents an higher distortion with respect to Sensor 2.</i>	30
3.15	<i>Radial distortion effect on 'Image_5.tif': on the left the distorted image is reported, with a barrel effect, on the right the undistorted image is presented. The latter appears perfectly calibrated.</i>	32
4.1	<i>Radiance parameters: θ represents the angle that the sensor forms with the normal direction, $d\omega$ is the corresponding solid angle and dA is the area framed by the camera.[15]</i>	34
4.2	<i>Radiometric calibration steps: the first one aims to convert DN values stored in memory in values of radiance/reflectance measured by the sensor. The second removes the atmospheric contributions leading to the real quantity related to the object.</i>	36
4.3	<i>Hypercube: x and y are spatial coordinates, while z is the spectral dimension. [16]</i>	38
4.4	<i>Spectral signature of the four Mapir target regions, therefore behavior of reference reflectances of Mapir panel in function of wavelength. The yellow curve is associated with the white region, the red one to the lighter grey, the light blue is related to the dark grey and the blue line to the black area.</i>	39
4.5	<i>ROIs selected in the image acquired with an integration time equal to 40 ms. The color code is the same described before.</i>	40
4.6	<i>DNs behavior versus wavelength: the average digital numbers for each region is plotted for each band. The curves are irregular.</i>	41

4.7	<i>Calibration line in band 14. Violet points are the four couples, while green ones are the corresponding values belonging to the line. They can be seen clearly as distinct.</i>	42
4.8	<i>Calibration line in band 84. Violet points are the four couples, while green ones are the corresponding values belonging to the line. In this case they coincide.</i>	43
4.9	<i>On the top RMSE representation, on the bottom R^2 both in function of wavelength. The behavior is uniform and presents optimum values except for the range [550 - 621]nm.</i>	45
4.10	<i>Calibrated reflectance values versus wavelength: for each band, average reflectance calculated with the LRM method is found in each target region. This behavior corresponds to the reference one.</i>	47
4.11	<i>RMSE for each image: the behavior is the same for each image but RMSE gets worse values as integration time increases.</i>	48
4.12	<i>R^2 for each image: the behavior is the same for each image but R^2 gets worse values as integration time increases.</i>	49
4.13	<i>Calibrated reflectances behavior along wavelengths: the top left figure is referred to the image 'Peronospora_1.bsq', acquired with an integration time equal to 30 ms; the top right plot is related to 'Peronospora_3.bsq' (integration time of 50 ms); the bottom left figure has been obtained for 'Peronospora_4.bsq' (integration time of 60 ms); the bottom right corresponds to the image 'Peronospora_5.bsq', acquired with an integration time of 70 ms.</i>	50
5.1	<i>Machine learning scheme: the initial step consists in training the algorithm with specific input data and leads to build a predictive model. Then, this model can be exploited to predict the new data given to the machine [17].</i>	51
5.2	<i>Training ROIs: several shapes are created for each class. The machine builds a model based on these indications, taking into account the spectral signature of the involved pixels.</i>	54

5.3	<i>SVM binary classes problem representation: an hyperplane divides the two datasets with the maximum margin from the support vectors. There are many other possible solutions to separate the two groups, but they are not optimal since they do not minimize errors.</i>	55
5.4	<i>RF representation: several subsets of training data are extracted and associated to a different decision tree. Each of them takes decisions and the final result is defined based on a major voting method, so considering the most frequent outcome of each tree.</i>	56
5.5	<i>Classified image 'Peronospora_2.bsq': on the left the result of classification performed with the SVM-500 algorithm is shown; on the right the outcome obtained through the RT-30,50,1000 method is visible. Color code is coherent with the Table 5.1</i>	57
5.6	<i>Classified image 'Peronospora_2.bsq': on the left SVM-0 classified outcome is reported; on the right the image elaborated with the RT-30,500,0 algorithm is shown.</i>	59
5.7	<i>Confusion matrix in case of two classes: the true values represent the points correctly classified, while false ones are associated to classification errors.</i>	60
5.8	<i>Accuracy points: 500 points are selected from two groups of ROIs, one used for training and the other for verification.</i>	61
5.9	<i>Confusion matrix 'Peronospora_2.bsq': on the diagonal the correctly classified points are indicated. The other cells contain the number of misclassified samples.</i>	62
5.10	<i>Porting on image 'Peronospora_3.bsq': both SVM and RF algorithms are employed, with the configuration indicated in the Table 5.2</i>	65
5.11	<i>Porting on image 'Peronospora_3.bsq': both SVM and RF algorithms are employed, with the configuration indicated in the Table 5.3</i>	66
5.12	<i>Porting on image 'Peronopora_5.bsq': the image represents the best case, obtained with SVM-500 method. The classification does not respect the real features.</i>	68
5.13	<i>Vineyard row represented with Mapir panel</i>	69

5.14 *Classification of a vineyard row: the image on the left is the result of the application of the SVM method, while the image on the right reports the classification performed with RT.* 70

Chapter 1

Introduction

Precision agriculture is the science of improving efficiency in fields employing advanced technology sensors and analysis tools, providing support to farmers in their business [18]. One of the main goals of this discipline is to observe the spatial and temporal variability of the factors that influence the agricultural production process, in order to improve the input efficiency in the dynamic management of the process. It means that a better solution can be found with the same amount of resources or the same solution with fewer inputs [19]. Therefore, there is a strong correlation between the fundamentals on which precision agriculture is based and the modern effort for reducing the environmental impact of agriculture.

This strategy is being adopted globally, in particular where technology is more advanced. At European level, several legislations are being made to provide standards and policies for precision agriculture applications. This aims to raise awareness of the themes of sustainability and climate change. In particular with the CAP 2014-2020 (Common Agricultural Policy), support is provided to precision agriculture: this field meets the measurements decided to focus the attention on resource exploitation, without excessive waste, and environment safeguard [20][21].

Agricultural systems dynamicity is taken into account since it is the origin of the variability of the responses to the productive factors. Temporal variability makes it possible that some operations can have different consequences during the years. Similar reasoning can be applied to spatial variability since different areas or cultures can react in different ways to the same intervention. It is important to monitor this variability and therefore to modulate the operations in order to improve and optimize processes results [19].

Hence, precision agriculture makes use of technology, which allows realizing the presented purposes. In the last years, digital innovations are playing a fundamental role in making agriculture a more competitive and sustainable field. Technological development is leading to new concepts, methods and tools that increase production efficiency [22].

Positioning systems, like Global Navigation Satellite Systems, allow a great accuracy in performing operations such as cultures management or autonomous navigation, relevant for precision agriculture.

Large improvements concern also sensor technologies. In particular optical sensors exploit remote sensing techniques to monitor plants status with a very high resolution such that nowadays it is possible to extract information from a single plant. They are able to detect radiations related to the object along all the electromagnetic spectrum, subdivided into several bands. Acquired and elaborated data can be easily exchanged through an internet network (IoT). With the evolution of wireless networks and transmission protocols, an increasing global interest is shown [22]. Since gathered information is generated in large volume, the rapid development of big data analysis and artificial intelligence is used to manage them [23]. Indeed, thanks to machine learning and deep learning methods, autonomous learning and decisions can be taken by the devices, providing large support to farmers. Hence the interaction between man and technology is becoming more and more substantial also in agricultural environments and many applications are being found to improve their management.

This thesis works in this context and the performed analysis is functional to reach the goals mentioned above. In particular, the used sensor is a hyperspectral camera that acquires images on ninety-seven bands. After subjecting them to calibration processes, with the purpose of making them independent of external factors, the calibrated images are then analyzed to apply several classification methods. In this specific case, the aim is to recognize the plant disease called Peronospora. Its principle is a fungus, called *Plasmopara viticola*, that affects vine leaves, but symptoms can occur also on grapes and branches. This leads to a loss in terms of products quality and cultures quantity, but also to a general decay of the cultures that become more susceptible to other diseases [24]. It is very important to limit the expansion of Peronospora in order to avoid these consequences and technology can help in this purpose.

All the steps are described in the current document following the structure indicated now. Chapter 2, "Material and Methods", reports the devices necessary for the work. In particular, details on the hyperspectral sensor used to acquire images on the field are explained and information about the Mapir panel is presented. Some theoretical concepts concern remote sensing and Peronospora vine disease. Then the implemented steps are described. Chapter 3, "Geometric Calibration", analyzes the operations performed on acquired images to remove distortions due to the camera; it is the first pre-processing applied method. Chapter 4, "Radiometric Calibration", reports the second pre-processing procedure applied to the acquired images. It is meant to remove any dependence on the external world of the information contained in the image. Chapter 5, "Classification", describes different methods to perform classification exploiting machine learning algorithms. The purpose is to train the machine to learn and recognize the Peronospora symptoms on vine leaves. The last chapter, "Conclusions", analyzes the final results and the possible evolution and applications of the project.

Chapter 2

Materials and Methods

The present chapter has the purpose of illustrating the basic concepts and principles on which this study relies, in order to introduce an extensive view and provide a scenario for this work. Moreover, several devices have been used to actuate the followed procedure: their functionality is described in this chapter.

2.1 Remote Sensing

Remote sensing is the process of detecting and monitoring the physical characteristics of an area by measuring its reflected or emitted radiation at a distance [25]. Sensors gather data and acquire images exploiting the spectral content of the radiation. They are typically mounted on satellites, drones or airplanes to observe the region below and characterize surfaces and objects. Thanks to the improvement of technology, this discipline is having a large success for several and different employments. Precision agriculture is one of the fields strongly supported by remote sensing: indeed, high resolution and precision are required in its applications, for example crop monitoring, irrigation, yield prediction nutrient application and disease treatment [23].

Analyzing the principles of remote sensing, it is important to specify and deepen the concept of electromagnetic spectrum. It represents the range of all the possible frequencies of the radiation, generated by the electromagnetic field, with the respective

energies. The higher the frequency ν associated with the wave is, the more significant the energetic content appears. The spectrum can be analyzed also in terms of wavelength λ , a parameter that is inversely proportional to the frequency. Seven regions can be identified, depending on the source of the waves and their effect on the materials:

- gamma-rays: $\lambda < 10 \text{ pm}$
- x-rays: $\lambda \in [10 \text{ pm}, 10 \text{ nm}]$
- ultraviolet: $\lambda \in [10 \text{ nm}, 400 \text{ nm}]$
- visible light: $\lambda \in [400 \text{ nm}, 750 \text{ nm}]$
- infrared: $\lambda \in [750 \text{ nm}, 1 \text{ mm}]$
- microwaves: $\lambda \in [1 \text{ mm}, 10 \text{ cm}]$
- radio waves: $\lambda > 10 \text{ cm}$

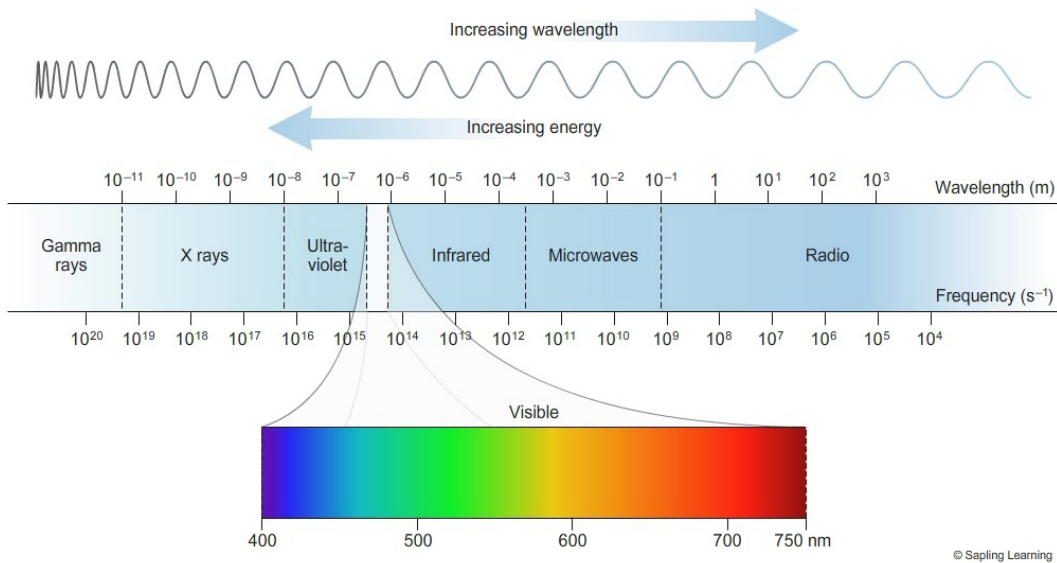


Figure 2.1: *Electromagnetic spectrum: representation of the bands ranges. Energy increases with frequency, inversely to the wavelength. [1]*

2.1.1 Sensors

Remote sensing is possible thanks to the use of sensors. These devices are able to detect the electromagnetic radiation reflected by the matter; this phase, followed by a post-processing procedure on acquired data, allows obtaining areas and objects information through the interpretation of spectral characteristics [16].

Sensor acquisition represents the first step of the explained process. Radiation reflected by an object is captured: depending on the exploited incident radiation source, a first distinction between sensors can be done [26]:

- passive sensors: the energy source is represented by the sun, which radiates the surfaces with all the frequencies of the electromagnetic spectrum. Another example of a natural source is related to the temperature of the target objects, which can be considered typically in infrared wavelengths. These characteristics make the acquisition strongly dependent on external conditions.
- active sensors: these sensors are able to transmit a light source or pulses, which represent the incident rays on the surfaces, and then they detect the reflected radiation produced by the targets. These devices are more complex than the previous ones since they need the equipment to provide the transmitting radiation.

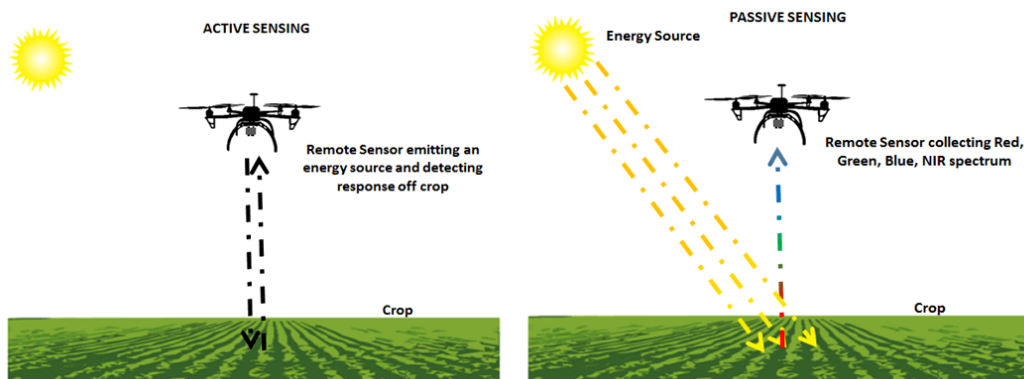


Figure 2.2: *Active vs passive sensors: on the left a representation of an active device is reported, which detects the reflected radiation that has been emitted by itself. On the right, an example of a passive sensor that exploits sunlight is represented.* [2]

When the wave is acquired, data pass through an elaboration step, where collection and normalization processes are applied in order to remove dependence on external factors such as atmospheric phenomena. This process leads obtaining the spectral signature, a curve that represents the radiation reflected by the surface with respect to frequency. Its variation in time and space is observed and interpreted allowing the identification of surfaces and areas under analysis. The creation of maps is also an application of this procedure [27].

The precision and detail level that a sensor can reach is related to the concept of resolution [28] [29] [30]. Four factors can influence the realized measurements:

- spatial resolution: it corresponds to the finite dimension of the pixel recognizable in the acquired image. The flight altitude is strongly related to this characteristic: systems more distant from the targets can not provide a high detail level.
- temporal resolution: it refers to the measurement of the frequency spent by the sensor to revisit the same part of the observation area, which in other words means the number of the same acquisitions in a defined time. This feature is related in particular to satellites applications.
- spectral resolution: it describes the width, and consequently the number, of the spectral bands captured by the sensor in the electromagnetic spectrum. The narrower the wavelength range is, the better the resolution becomes and the information detailed.
- radiometric resolution: it is related to the number of bits used to record the radiation information. Indeed, the number of discrete levels that describe the object raises as the number of bits increases. This is related to better sensor resolution.

$$L = 2^{Nb}$$

Depending on the number of acquired bands, there are four techniques to obtain data from a given target [22] [3] :

- RGB sensors: they work in the visible light range of the spectrum, typically represented by red, green and blue bands. This technique is not enough to provide certain physical and chemical properties, therefore its use is limited to few applications.
- multispectral sensors: they work in some spectral bands, typically from 5 to 10, in the range 400-1000 nm. The spectral resolution is not optimal yet, bandwidth is of the order of 100 nm.
- hyperspectral sensors: these cameras are used when a high spectral detail level is required. Indeed, more than 100 bands can be acquired, since the width of each band is of the order of some nm. They allow capturing object properties that are not visible to the human eye. As a consequence, more applications can be found.
- thermocameras: they work in the thermic infrared (7500-13500 nm) and are able to map object temperature so that each pixel value is related to the temperature of the section.

Hyperspectral sensors can sense the physical and chemical parameters of a specimen with a higher level of detail. Depending on the acquisition mode, different types can be distinguished [3].

- point scanning (BIP): it acquires images pixel by pixel storing information interleaving bands. Therefore a band interleaved by pixel cube is obtained.
- line scanning(BIL): it works similarly to the BIP method but is proceeds line by line instead of pixel by pixel.
- plan scanning (BSQ): it acquires all the x-y pixels and stores the entire plan for each band.
- single shot: it acquires all the spatial and spectral information at a once. It is a more recent technique.

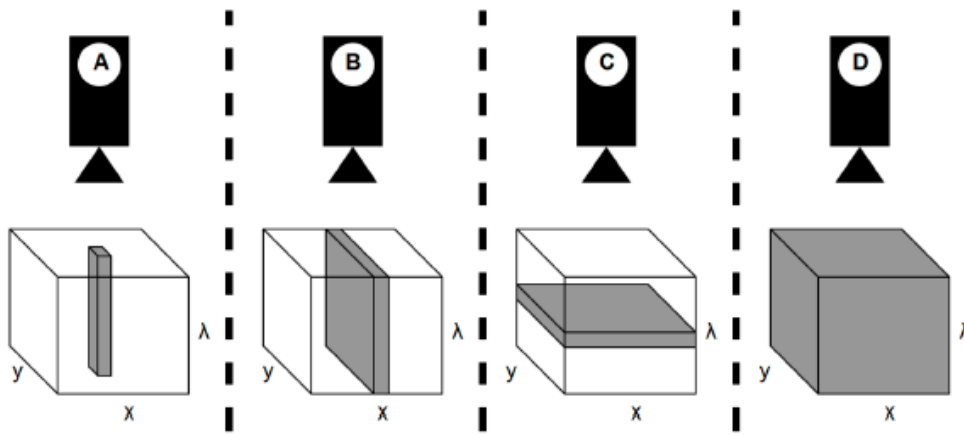


Figure 2.3: *Acquisition modes: in the drawings, x and y are the spatial coordinates of the pixels, while λ is referred to the wavelength axis. Figure A corresponds to a BIP mode, Figure B to a BIL technique, Figure C represents BSQ and Figure D corresponds to SS [3]*

2.1.2 Hyperspectral camera Rikola

The hyperspectral camera Rikola is the sensor employed for the project. This device is designed by the VTT Technical Research Centre of Finland and produced by Senop [14].



Figure 2.4: *Rikola hyperspectral camera from DIATI at Politecnico di Torino*

It is composed of two different CMOS sensors [31]: the former works on bands in the near-infrared (NIR), from 643 nm to 902 nm, while the latter acquires part of the bands in the visible light, from 505 nm to 636 nm.

Another important component is the Fabry-Perot interferometer: this device is represented by two parallel partial reflective surfaces that form a cavity, called air gap, between them. The distance can vary and it is controlled by piezoelectric actuators [14]. When the electromagnetic radiation hits the first plate, it is partly reflected and partly transmitted. The latter component enters the cavity and the same behavior occurs when it affects the second plate. A series of reflections starts in the cavity and the different waves sum up based on their phase.

There can be two extreme conditions: constructive interference, when the radiations are in phase and are totally transmitted through the surface, and destructive interference, when the waves are out of phase and null themselves. Hence it is a selective process since only specific frequencies can pass over. In particular, this condition occurs when a precise relation between wavelength and cavity length is respected [32].

$$N \cdot \lambda = L_c, \quad N = 1,2,3$$

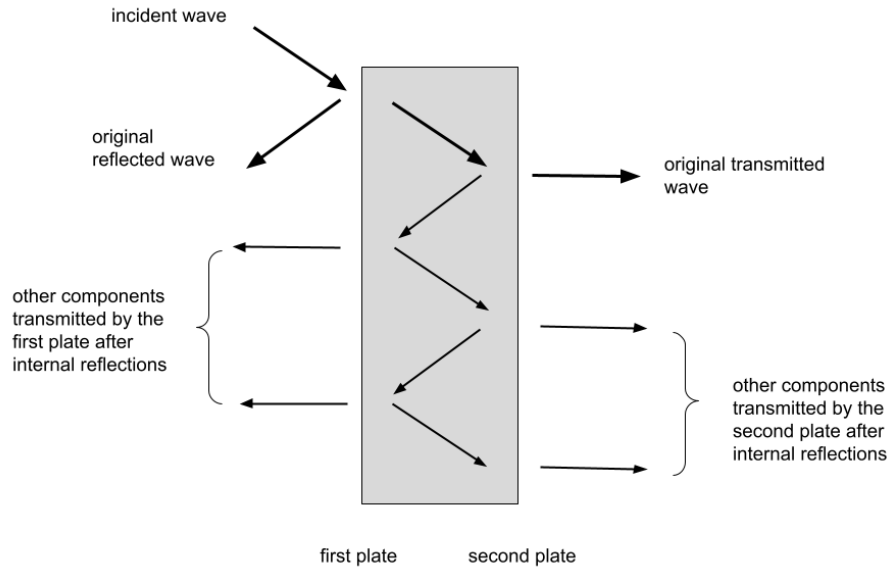


Figure 2.5: *Fabry Perot interferometer: in the cavity formed by the two plates several reflections occur and only specific components are transmitted out of it.*

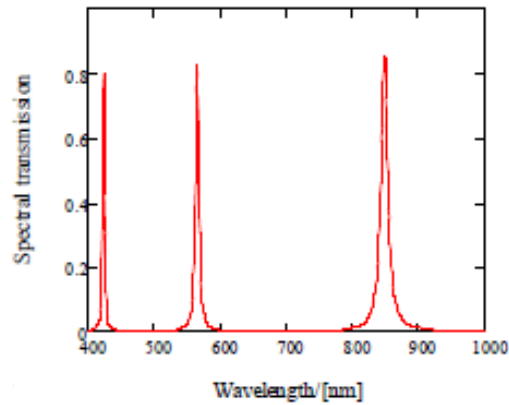


Figure 2.6: *Fabry Perot interferometer modes: only specific wavelengths can be transmitted. The selected ones depends on the cavity length. [4]*

Those wavelengths are in resonance with the cavity, the others are eliminated. Varying the distance between the plates, the resonant wavelength changes.

Hence, the radiation passes through the optical assembly, it is filtered with the interferometer and then it is directed to one of the two CMOS sensors. Rikola hyperspectral camera is also provided with a GNSS receiver for georeferencing purposes and with an irradiance sensor used for radiometric calibration.

For this study, the camera has been used to acquire images along 97 bands, from 505.84 nm to 902.39 nm. The spectral resolution is therefore about 4 nm. Image dimension is 1010 x 1010, data are stored in floating-point notation and the acquisition is in DAT format.

2.2 Peronospora

In this thesis work, images that represent vine leaves affected by Peronospora are captured through sensors. Peronospora is a typical vine disease that can cause huge damages to cultures and farmers' business. The causal agent is the *Plasmopara viticola*, a fungus that originated from North America and lives mainly in humid areas. It is characterized by a polymorphism of its spores [5], therefore the biological cycle of the *Plasmopara viticola* includes a sexual stage and an asexual stage: the former ensures the survival of the pathogen over winter and is related to the primary infection in spring, while the latter is responsible for the successive secondary infection cycles that occur in the host-growing season [33]. The entire life of his pathogen is strongly influenced by external meteorological conditions, indeed humidity plays a fundamental role in the fungus generation and survival. The temperature must be relatively high in the infection phases and abundant rainfalls must occur: thanks to the wind and rainwater the spores infect the cultures.

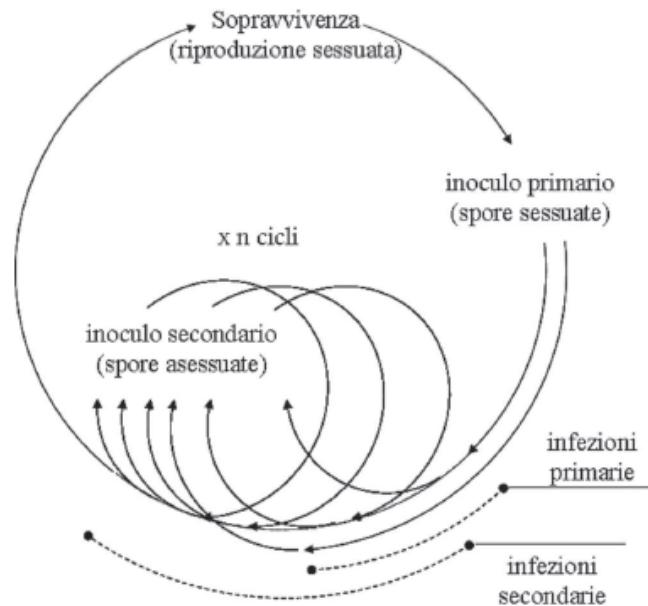


Figure 2.7: Representation of the *Plasmopara viticola* life cycle: after the primary infection, other multiple secondary infections can occur. Then the survival stage during winter. [5]

When the plant is affected by the *Plasmopara viticola*, symptoms can appear on all the herbaceous organs. In particular, leaves start showing several spots on the upper side: they can be quite big, yellow and translucent, called oil spots, or smaller, chloritic and located especially on veins, organized as in a mosaic [6]. In the lower side of the leaf, in correspondence with these spots, a white mycelial felt appears, mainly in conditions of high humidity. The consequence of this pathology is leaf necrosis, desiccation and the premature fall.

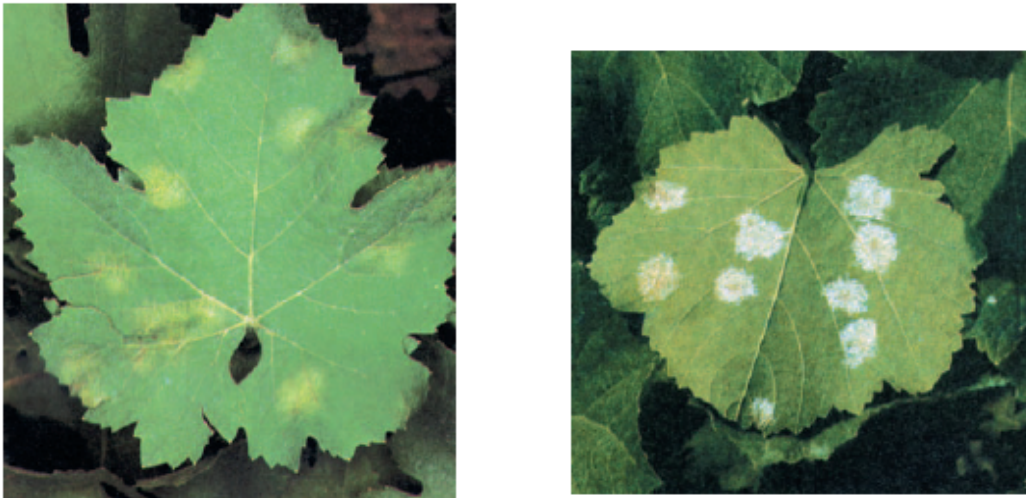


Figure 2.8: Representation of *Peronospora* effects on vine leaves: on the left oil spots in the upper side are shown, on the right oil spots in the lower side [6].

Plasmopara viticola can also attack grapes and branches, causing their browning, curvation and the development of the white mold.

It is easy to understand that such disease generates a lot of problems and damages: first of all a general decay of the plants' health occurs, plants which become more susceptible to other diseases. As a consequence, worse quality of produced wine is encountered, but in the worst cases, a huge loss in terms of vine plants quantity is caused [6].

Therefore, it is important to limit the diffusion of the *Peronospora* in the vineyards by applying the correct products to fight it. The preventive actions to avoid its appearance consist especially in applying uniformly and externally fungicides that act in contact with the plant: this treatment must be done before the infection begins, so that a chemical barrier is formed. If the fungus is already present, curative substances are used that are able to penetrate the plant tissues and stop the incubation of *Plasmopara viticola* [6].

It is important to avoid overexploitation of these phytosanitary products: environment sustainability is becoming a fundamental concept and the excessive use of chemical substances goes against this practice. It is necessary to localize the problem and adopt precision strategies to fight diseases without affecting the environment and wasting resources. Precision agriculture is as a consequence a fundamental field that is developing very fast thanks to the help of technology.

2.3 Mapir

The images acquired for this study represent vine leaves affected by *Peronospora*. Before proceeding with the classification, images must be calibrated. In particular, one step is the radiometric calibration, which aims to convert the information contained in the image as Digital Numbers in terms of radiation reflected by the surface. This is necessary to obtain normalized values such that external parameters do not influence the measurements.

In order to apply this technique, a target object is needed in the acquisitions, whose surface reflected radiation values are known.

The target object is represented by the Mapir panel [7], whose dimensions are 31.75 x 25.4 x 3.18 cm. It is composed of four regions in felt of different colors mounted on plastic support: black, dark grey, light grey, white.

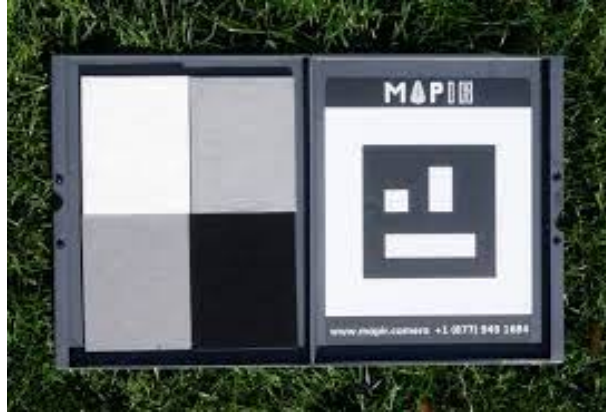


Figure 2.9: *Mapir panel: target object with reference values [7]*

Reflectances corresponding to these four regions have been measured in a previous phase with a spectrophotometer and used as reference values. Thanks to the target material's diffuse properties, any camera orientation during acquisition is valid for good results. Indeed, the Mapir panel is a Lambertian surface, which means that reflects the incident light homogeneously in all directions.

Chapter 3

Geometric Calibration

The image acquisition through a sensor is usually followed by pre-processing procedures. One of them is the geometric calibration, which will be illustrated in this chapter: indeed, cameras produce distortions on the captured image.

Geometric calibration aims to determine the geometric properties of the used camera, such as intrinsic and extrinsic parameters, which will be explained in the first section to better understand the nature of the distortion. After this step, the correction of the images can take place, taking into account the sensor characteristics. All the followed steps will be shown in the proper section of this chapter.

3.1 Camera Parameters

The algorithm to determine camera parameters is based on the model proposed by Jean-Yves Bouguet, which takes into account a pinhole camera model and lens distortions [9]. Indeed, an ideal pinhole camera does not have lenses and therefore it does not include a distortion model. In order to represent a more real camera, the latter must be considered.

A pinhole camera is a simple camera that does not have lenses but presents a single small aperture. Light rays pass through the aperture and project an inverted image on the opposite side of the camera [9]. The pinhole camera parameters are represented in a matrix, called camera matrix, which maps the 3D object in a 2D image. It includes extrinsic and intrinsic parameters: the former represent a rigid

transformation from the 3D world coordinate system to the 3D camera coordinate system, while the latter represent the projective transformation from the 3D camera coordinates into the 2D image [9].

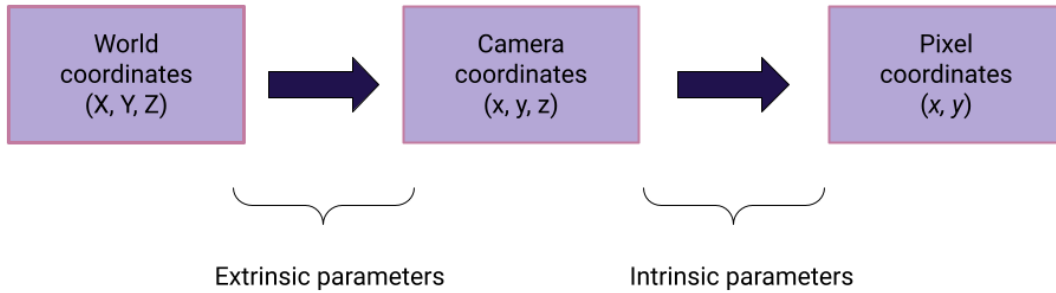


Figure 3.1: *Extrinsics and intrinsics transformation: from 3D to 2D. External parameters connect the 3D coordinates of the real world and the camera. The transformation in the 2D dimension is performed by the intrinsic parameters.*

Hence, in order to perform this operation, equations that relate the real and physical world to the virtual one represented in an image are needed [9].

$$w[x \ y \ 1] = [X \ Y \ Z \ 1]P$$

The first vector contains the image coordinates and the second vector represents the world coordinates. Analyzing the other parameters that appear in the equation, the variable w is a scale factor, while P is constituted by the following quantities:

$$P = [R \ t]K$$

K represents the intrinsic matrix that contains all the intrinsic parameters and R and t are respectively extrinsic rotation and translation.

All these parameters are explained in detail in the following sections.

3.1.1 Intrinsic parameters

As explained before, intrinsics are those parameters that connect the pixels coordinates to the coordinates system of the camera [34].

It is necessary to consider the situation in the figure below.

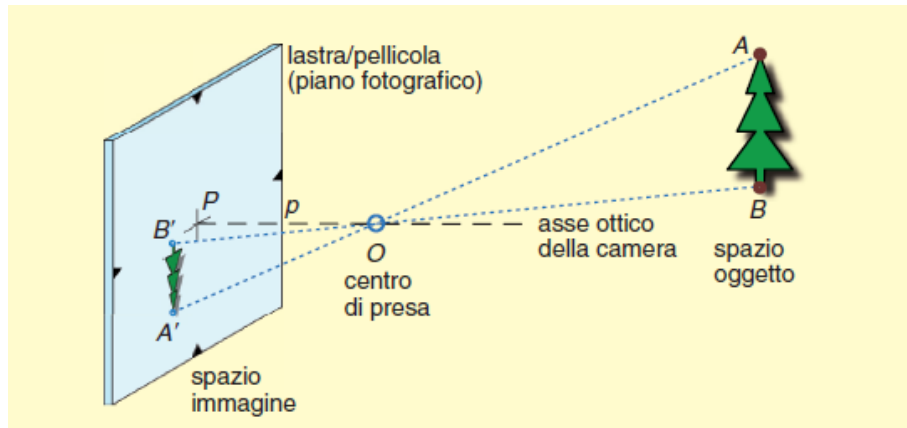


Figure 3.2: *Transformation of the real object in an image. Relation between object space and image space* [8]

An image space is associated to the real space. Each point of the framed object (A, B) corresponds to a point in the image space (A', B'). If straight lines are traced to connect the point couples, they all meet in a single point O called perspective center. Its projection on the image plane is the principal point (P). The distance between the perspective center and the image plane is the focal length [8]. Principal point and focal length are two intrinsic parameters: they are both expressed in two coordinates in the intrinsic matrix, considering the x and y components and the former is usually at the center of the image.

The other intrinsic is the skew, which represents how much the two axes are not perpendicular.

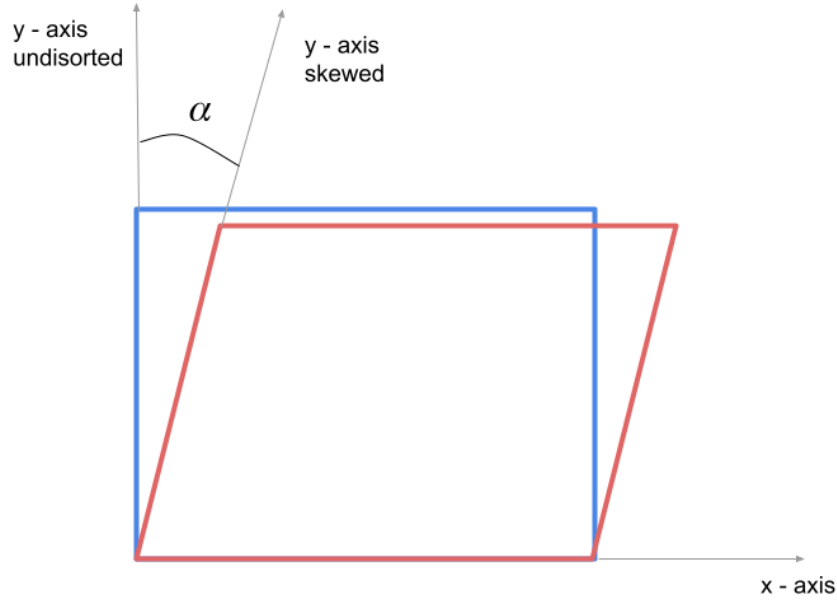


Figure 3.3: *Skew representation: the blue drawing represents the original pixel matrix, where x and y axis are perfectly perpendicular. The red rectangle shows the effect of the skew parameter, since the two axes are not orthogonal.*

The intrinsic matrix results like this:

$$\begin{bmatrix} f_x & 0 & 0 \\ s & f_y & 0 \\ c_x & c_y & 1 \end{bmatrix}$$

where c_x and c_y are the coordinates of the principal point, f_x and f_y are the focal distance normalized with respect to the pixel dimensions and s is the skew.

$$f_x = F/p_x \qquad f_y = F/p_y \qquad s = f_x \cdot \sin(\alpha)$$

3.1.2 Extrinsic parameters

Extrinsics define the position and orientation of the coordinate system of the camera with respect to the coordinate system of the world [34].

In order to describe the relation between these two reference systems, a rotation matrix 3×3 and a translation vector 3×1 are used. The center is the principal point.

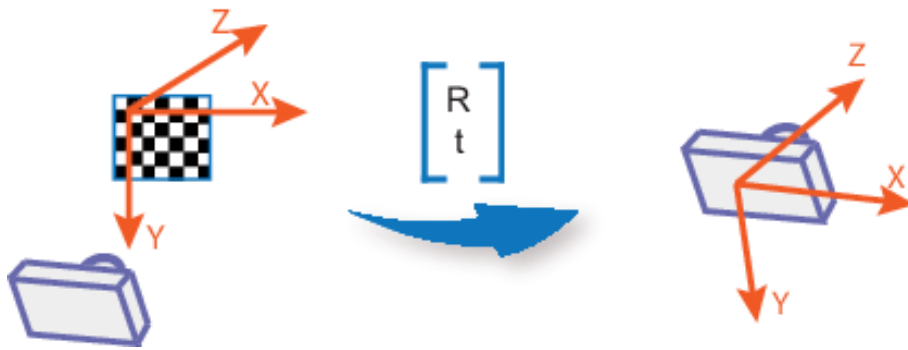


Figure 3.4: *Extrinsics: rotation and traslation are applied passing to the camera coordinate system. [9]*

3.1.3 Distortion coefficients

These are intrinsic parameters due to the presence of lenses that do not take part in the intrinsic matrix since the ideal model does not include lenses. But for a real and complete scheme, they must be considered.

The first contribution is the radial distortion. It occurs when light rays bend more near the edges of a lens than they do in the center. It is described through three coefficients, k_1 , k_2 , k_3 that relate the ideal coordinates to the distorted ones:

$$\begin{aligned} x_{\text{distorted}} &= x_{\text{undistorted}} \cdot (1 + k_1 \cdot r^2 + k_2 \cdot r^4 + k_3 \cdot r^6) \\ y_{\text{distorted}} &= y_{\text{undistorted}} \cdot (1 + k_1 \cdot r^2 + k_2 \cdot r^4 + k_3 \cdot r^6) \end{aligned}$$

where r is the radial distance ($\sqrt{x^2 + y^2}$) and x and y are the pixel coordinates translated to the optical center and normalized with respect to focal length [9].

Depending on the sign of the radial distortion, different effects can affect the image: if it is negative, a barrel effect is obtained, otherwise, if it is positive, a pincushion behavior is visible [35].

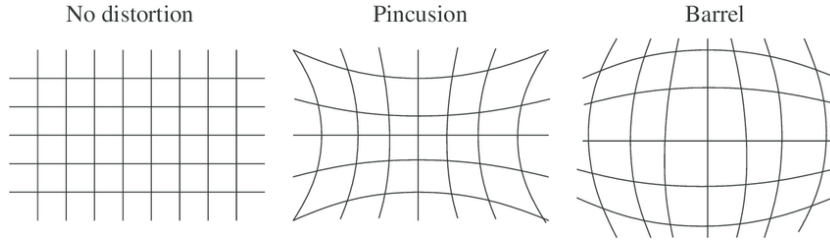


Figure 3.5: *Effect of radial distortion: on the left the image not affected by distortion is represented; the center figure shows the barrel effect that characterizes the image; on the right pincushion effect affecting the image is shown. [10]*

Considering the radial distortion behavior to the variation of radial distance, the typical curves are shown below.

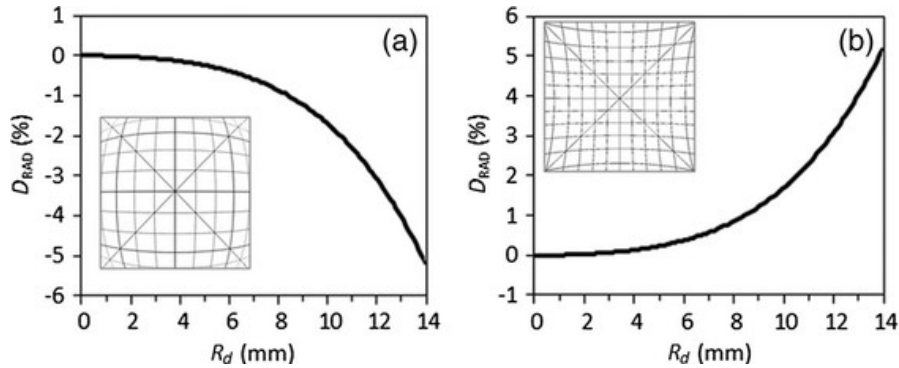


Figure 3.6: *Radial distortion behavior: on the left a typical barrel behavior is presented, characterized by negative values of the distortion parameter; on the right the pincushion behavior with radial distance is shown, characterized by positive values of the radial distortion [11]*

The second contribution, usually negligible, is the tangential distortion, which occurs when the lens and the image plane are not parallel.

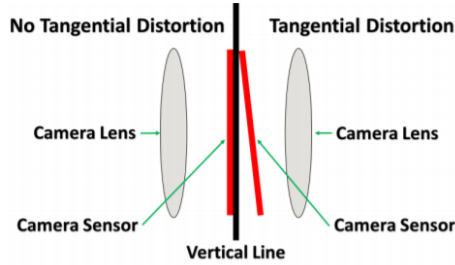


Figure 3.7: *Tangential distortion is caused by a missed alignment of the sensor with respect to the lens [12]*

The phenomenon is described through two coefficients p_1 , p_2 that are used in the equations to model the distortion:

$$x_{\text{distorted}} = x_{\text{undistorted}} + [2 \cdot p_1 \cdot x \cdot y + p_2 \cdot (r^2 + 2 \cdot x^2)]$$

$$y_{\text{distorted}} = y_{\text{undistorted}} + [p_1 \cdot (r^2 + 2 \cdot y^2) + 2 \cdot p_2 \cdot x \cdot y]$$

Both the distortion contributions can be represented as in the Figure 3.8: the radial distortion produces a shift of the points in a radial direction, while the tangential distortion moves the point along a circumference arc.

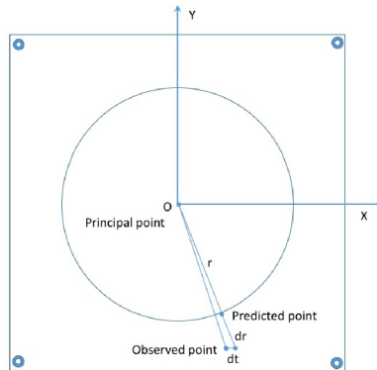


Figure 3.8: *Radial and tangential distortion effect: the observed point does not correspond to the predicted one. [13]*

3.2 Image acquisition

In this thesis work, the geometric calibration is applied to a set of 13 images acquired in the Laboratorio Di Fotogrammetria, Geomatica e GIS in the DIATI(Dipartimento di Ingegneria dell’ambiente, del Territorio e delle infrastrutture) at the Politecnico di Torino. The operation has been performed in an indoor environment with uncontrolled light conditions. It is important to underline that the named images do not represent the core of this study, so the Peronospora phenomenon; indeed, the purpose is to describe the procedure and the fundamental steps to perform the geometric calibration and comment the obtained results.

The acquisition is performed connecting the camera to the USB port of a computer. Thanks to the use of the software HyperSpectralImager v2.1.4, it was possible to select the image resolution and the number of bands, therefore the spectral resolution. Moreover integration time has been set according to the illumination condition of the environment. All these characteristics are summarized in the table below.

Image resolution	1010 x 1010
Pixel dimensions	5.5 μm
Number of bands	97
Spectral resolution	4 nm
Range of bands	[505.84, 902.39] nm
Integration time	1200 ms

Table 3.1: *Acquisitions settings*

A preliminary operation is the dark current test, necessary when a new integration time is set to estimate the effect of temperature. A black and small panel covers the camera lens so that light is not sensed.

The acquisitions have been made framing a checkerboard panel whose minimum square is 10 cm long.



Figure 3.9: *Checkerboard panel: it is the object of the acquisitions.* [14]

Several frames have been adopted to capture the panel: five images were taken placing the sensor almost at the same height of the floor and five considering the camera at a height equal to about 1.50 m. The five positions were obtained by moving the Rikola device to the extreme left of the panel and then to the left, center, right and extreme right. Then the sensor was settled at an intermediate height between the two selected before and 3 images were taken: left, center, right.

3.3 Procedure

Camera parameters include intrinsic, extrinsic and distortion coefficients. In order to estimate the camera parameters, it is necessary to have 3D world points and their corresponding 2D image points. These correspondences can be gotten using multiple images of a calibration pattern, such as a checkerboard [9].

This thesis work aims to evaluate the intrinsic parameters of the hyperspectral camera Rikola in order to correct the hyperspectral images and remove the distortions due to the device.

The images have been acquired in DAT format and converted in TIF format in order to be elaborated. The operation has been performed exploiting the ENVI software that is able to open DAT files.

The following steps have been executed in MATLAB R2021a and can be identified in:

- bands separation for each image
- camera parameters estimation for each band
- elaboration of the obtained parameters
- calibration of each band
- reconstruction of the images combining all the bands

3.3.1 Bands separation

Each TIF image contains information on 97 bands, but, for geometric calibration purposes, each band must be processed separately. In this way, a more consistent estimation of the camera parameters can be obtained. Therefore a first operation consists in dividing each image into bands and saving each band as a TIF file.

3.3.2 Camera parameters estimation

In order to proceed with the other steps, a Matlab application, called Camera Calibrator, is used. It requires the package Image Processing and Computer Vision and is able to estimate the camera parameters starting from an image as input. The provided code is extended according to the project specifications.

In particular, the functions work on one set at a time of images belonging to the same band: therefore each set is composed of 13 images, one for each acquisition, and the total number of sets is 97, corresponding to the number of bands.

The algorithm detects a checkerboard pattern in the group of images provided as an array of files, based on the square size of the panel, and then generates checkerboard corners location in the world reference system.

Camera parameters are therefore estimated: in particular, both extrinsic and intrinsic quantities are provided, but also distortion coefficients.

3.3.3 Camera parameters elaboration

Regarding the extrinsic quantities, a 3D visualization is provided: in particular, two types of view can be requested. One is called pattern-centric, which shows the several positions of the camera with respect to the panel, whose location is maintained fixed. The other is camera-centric, which instead represents the pattern position with respect to the camera which remains in the same location. In this case, the real acquisition corresponds to the pattern-centric mode.

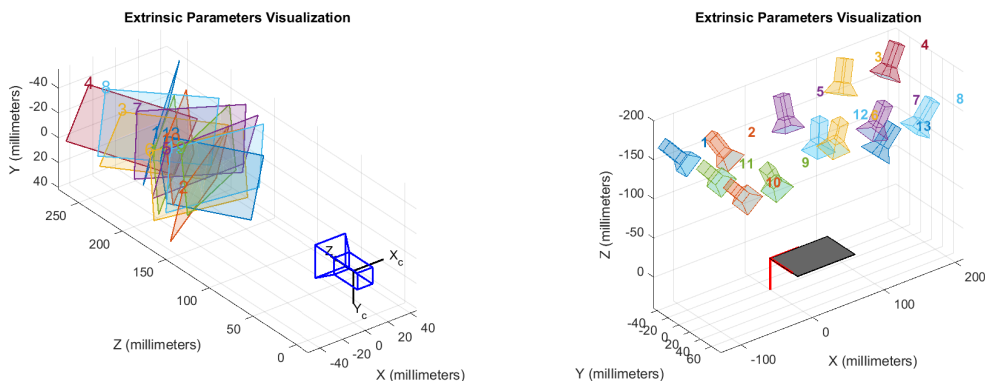


Figure 3.10: *Extrinsics*: on the left camera-centric view is shown, hence all the panel positions with respect to the camera appear. On the right pattern-centric configuration is represented: it corresponds to the performed case.

In this study, more attention is paid to the intrinsics: principal point and focal length are reported in pixel measurement unit and both with an x and y component. For the principal point, it is an intuitive notation; regarding focal length, it is used since the reported value is actually the focal length normalized with respect to the two pixel's dimensions.

It is possible to choose whether the skew calculation is needed, as well as the tangential distortion coefficients. Moreover, the number of coefficients that describe the radial distortion can be decided (2 or 3). In this study, all these parameters are calculated for each band and some analysis is performed.

Considering the focal length, the average value in mm between the x and y component is computed and its behavior with bands variation is plotted, as shown in the Figure 3.11.

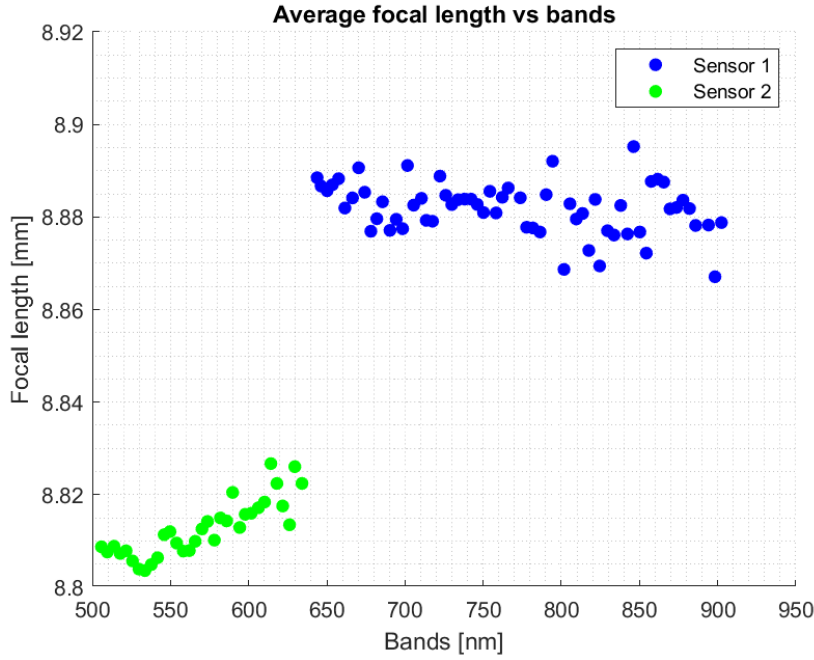


Figure 3.11: *Focal length vs wavelength: two distinct groups are visible. The blue points are referred to Sensor 1, the green ones to Sensor 2*

As visible, two separated groups of points can be identified in the graph. This is due to the presence of two sensors in the Rikola hyperspectral camera. Indeed, they present slightly different features, that are clearly distinct here. The blue points refer to Sensor 1 and their values belong to the range $[8.8-8.83]$ mm; the green points are associated with Sensor 2 and are in the interval $[8.86-8.9]$ mm.

Regarding the principal point, the performed analysis consists in plotting the two components, y in function of x , considered in mm. The y component is called η_0 , while the x component is written as ξ_0 .

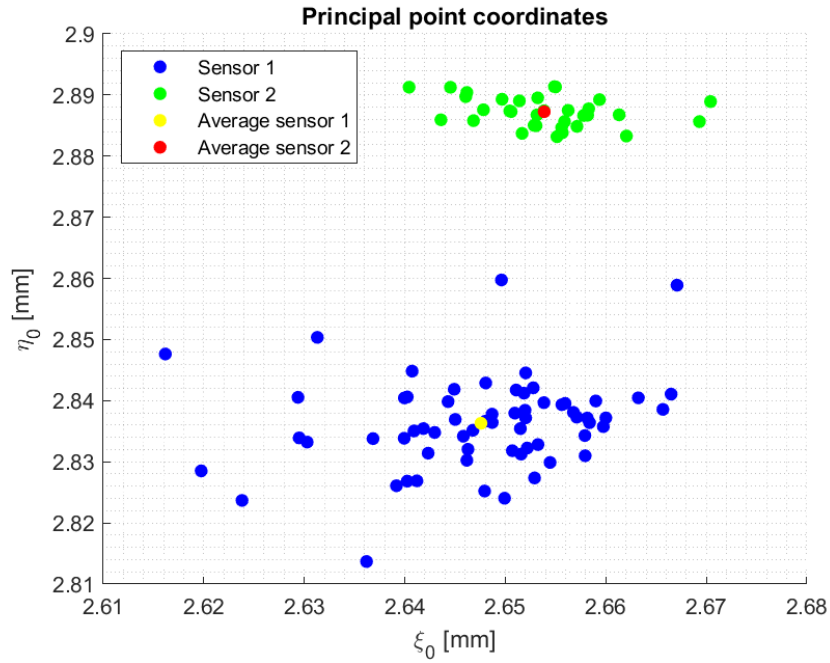


Figure 3.12: *Principal point vs wavelength: two groups can be identified. The blue ones characterize the Sensor 1 and are more spread around the average value, while the green set is referred to the Sensor 2 and appear more compact.*

The figure shows that they are organized into two clusters. The blue ones belong to Sensor 1, while the green ones to Sensor 2: average values are therefore slightly different and correspond respectively to 2.835 mm and 2.885 mm. Points associated with Sensor 1 are more spread and present more different values among them.

The last intrinsic parameter that appears in the intrinsic matrix is the skew. Verifying its behavior against bands, it can be noticed that there are no evident differences between behavior characterizing Sensor 1 and Sensor 2.

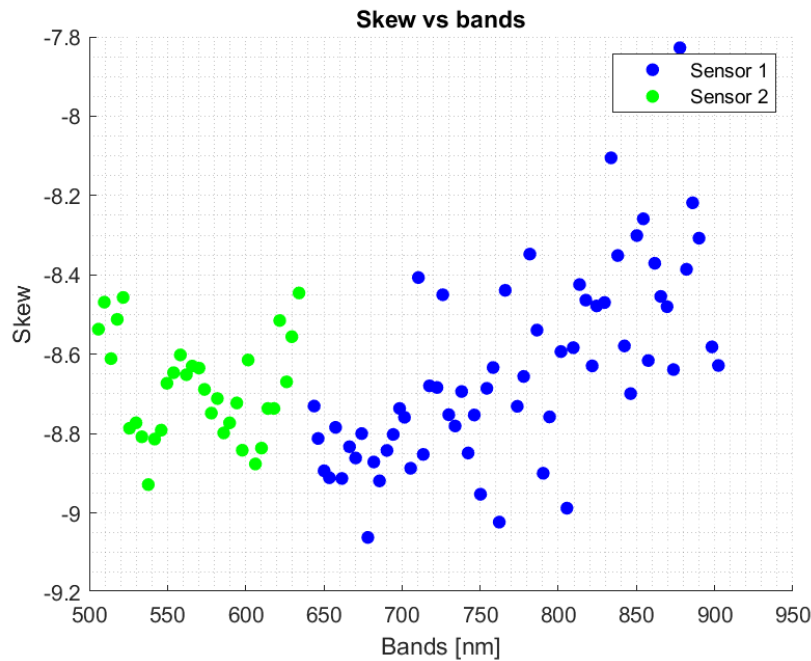


Figure 3.13: *Skew vs wavelength: blue points belong to Sensor 1, green points to Sensor 2. No great differences between the two groups are visible.*

Further studies can be performed on distortion coefficients. In particular, only radial distortion is taken into account in this analysis since the tangential one is very small and can be considered negligible.

The radial component affects mainly the edges of an image. For verifying this behavior, it is plotted against the distance of each pixel from the optical center.

It is necessary to previously define the radial distance, expressed, for each sensor, as

$$r = \sqrt{\left(\frac{dx}{f_x}\right)^2 + \left(\frac{dy}{f_y}\right)^2}$$

where f_x and f_y are the averages between all the bands, distinct for the two sensors, of the focal length in pixel values given by the calibration, and dx and dy the pixel distances.

Therefore the radial coefficient has been calculated for each sensor as [14]:

$$f_r = k_1 \cdot r^3 + k_2 \cdot r^5 + k_3 \cdot r^7$$

where the k_1 , k_2 , k_3 are the averages between all the bands of the obtained coefficients, considering the two groups related to each sensor.

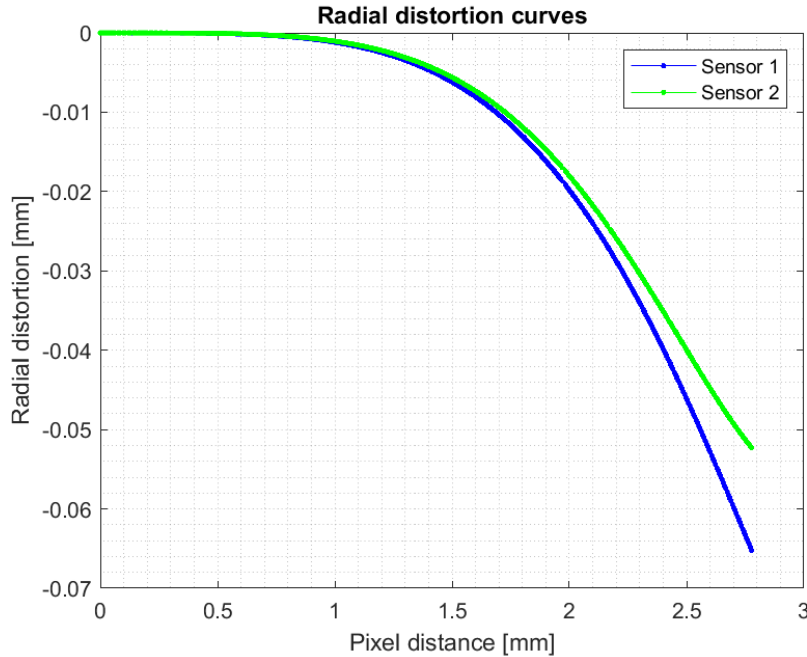


Figure 3.14: *Radial distortion vs pixel distance: a behavior typical of barrel effect is visible. As the pixel is near to the edge (i.e. pixel distance increases), the distortion is more visible. Sensor 1 presents an higher distortion with respect to Sensor 2.*

As the theory says, when the pixel distance from the principal point increases, the radial distortion becomes higher in absolute value. Going towards the edges and farther from the center, the distortion is more markable. Since the assumed values are negative, the encountered effect is the barrel one.

Sensor 1 is more affected by this effect with respect to Sensor 2 as the distance from the principal point increases. In particular, the difference between the two curves becomes evident starting from a pixel distance equal to about 2 mm.

3.3.4 Bands calibration

In order to proceed with calibration, all the averages of the parameters computed by CameraCalibrator are calculated, considering separately the two sensors. Two groups of 33 and 64 bands appear. The new averaged intrinsic matrices and distortion coefficients, all expressed in pixels, are:

$$\begin{bmatrix} 1613.4 & 0 & 0 \\ -8.6304 & 1616.6 & 0 \\ 481.3779 & 515.6912 & 1 \end{bmatrix} \quad \begin{bmatrix} 1600.6 & 0 & 0 \\ -8.6848 & 1604.6 & 0 \\ 482.5213 & 524.9574 & 1 \end{bmatrix}$$

	k_1	k_2	k_3	p_1	p_2
Sensor 1	-0,2793	-0.6086	3.3157	-6.8774e-4	-7.3456e-4
Sensor 2	-0.2315	0.9319	5.1693	-0.0013	-8.3325e-4

Table 3.2: *Averaged intrinsic parameters: on the left top intrinsic matrix of Sensor 1 is reported, on right top intrinsic matrix of Sensor 2, on the bottom table with distortion coefficients for both Sensors. All the values are averaged quantities.*

The correction of each image is performed exploiting these new parameters and band by band. The first 33 bands are calibrated with the parameters of Sensor 2, the others with quantities proper of Sensor 1. In this way, the new images do not present the effect of distortion.

As an example, band 20 of the 'Image_5.tif', acquired from an height of about 1.50 m and from the center. is reported below:

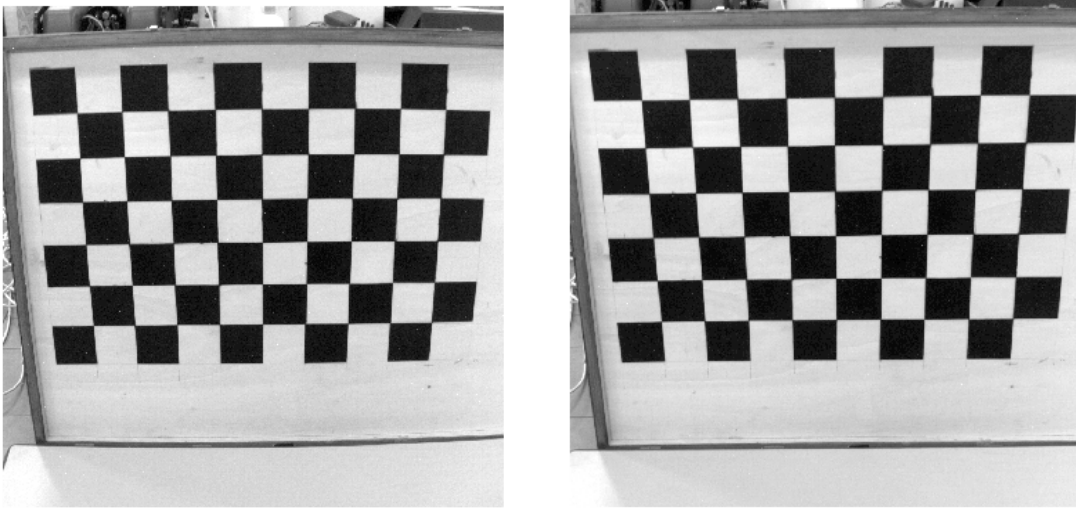


Figure 3.15: *Radial distortion effect on 'Image_5.tif': on the left the distorted image is reported, with a barrel effect, on the right the undistorted image is presented. The latter appears perfectly calibrated.*

A great difference can be noticed comparing the before and after calibration images.

3.3.5 Bands combination

After this operation, the obtained calibrated images are combined in order to constitute the 13 images that contain information on 97 bands. The recording is performed considering the TIF format, with single precision and in big-endian machine format.

Chapter 4

Radiometric Calibration

The second pre-processing method consists of radiometric calibration. When images are acquired, they can be susceptible to environmental conditions: different contributions, like sensor noise and atmospheric scattering and absorption, can introduce noise and errors in the captured images. Therefore, the detected information, stored as Digital Numbers, is not the direct measurement of the radiation: it depends on external conditions and can change with illumination and sensor consistency. The radiometric calibration aims to convert DNs to surface reflectance values, making quantitative the analysis in cases of images acquired with different sensors or at different times of the day [36].

In this chapter, all these concepts are analyzed in depth, explaining the required basics at the beginning. The followed procedure to calibrate the images is then illustrated.

4.1 Digital Numbers, Reflectance

Hyperspectral sensors acquire the spectral characteristics of Earth's surface in many narrow and contiguous bands [37]. When solar radiation hits a surface, the material reflects part of the incident radiation. The parameter that describes this phenomenon is the radiance, which can be defined as the amount of the radiation reflected by a surface of a unitary area towards a unitary solid angle and in a direction orthogonal to the observation point [38].

As visible, it depends on the observation geometry.

$$L = \frac{d^2\Phi}{d\Omega \cdot dA \cos\theta}$$

where:

- $d^2\Phi$ is the quantity of electromagnetic energy transported by the wave per unit time between two surfaces.
- dA is the detected area by the sensor
- $d\Omega$ is the solid angle in which the sensor detects the radiation
- θ is the angle between the specific direction and the normal to the surface

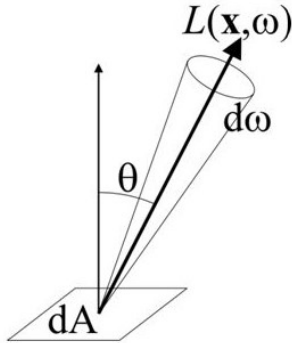


Figure 4.1: *Radiance parameters: θ represents the angle that the sensor forms with the normal direction, $d\omega$ is the corresponding solid angle and dA is the area framed by the camera.*[15]

Another quantity that expresses the same concept but in a relative way is introduced in this analysis, the reflectance. It represents the reflected power captured by the sensor with respect to the incident power on the surface. It is defined as:

$$\rho = \frac{\phi_r}{\phi_i}$$

It is a normalized value, included in the range $[0,1]$.

When the sensor acquires the radiation, it is stored in a digital image format, constituted by a pixel matrix. In particular, the radiation information is translated into a Digital Number. It is associated with each pixel of the image and corresponds to the detected energy level, which can be translated into a grey level. The number of levels depends on the radiometric resolution, therefore on the number of bits used for encoding the information. Hence, each pixel has three information: the two variables x and y that locate it into the matrix and the DN which identifies the grey shade [38]. In the case of hyperspectral sensors, many matrices are obtained, one for each band, and each pixel has a vector of associated DNs, as many as the number of bands.

4.2 Procedure

Ideally the radiance, and so the reflectance, captured by the sensor is equal to the effective one emitted by the surface, but, in reality, the measurement is affected by other phenomena such as absorption and scattering of atmosphere and is the result of all these contributions [37]. Moreover, when the measurement is converted by an ADC in a digital quantity, some errors can occur relatively to the device characteristics. It is very important to correct these aspects since spectral behavior of radiance/reflectance, therefore object spectral signature, is the key for understanding surface properties and characterizing them.

The radiometric calibration aims to perform this operation in order to estimate correctly the reflectance removing external dependencies. It consists mainly of two steps [39]:

- sensor calibration
- atmospheric correction

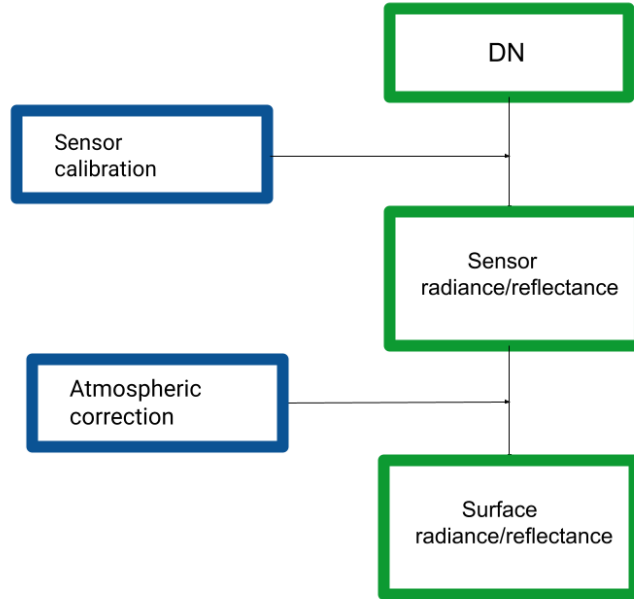


Figure 4.2: *Radiometric calibration steps: the first one aims to convert DN values stored in memory in values of radiance/reflectance measured by the sensor. The second removes the atmospheric contributions leading to the real quantity related to the object.*

The process regarding the hyperspectral images acquisition through a sensor has as input the radiance related to the observed scene and as output the corresponding DN stored. The sensor calibration aims to find the input radiance/reflectance measured by the sensor based on the output information taking into account imperfections introduced by the sensor.

The calibration relation that connects the radiance/reflectance at the sensor to the DN quantity can be expressed as:

$$L_{\lambda} = of f_L + gain_L \cdot DN$$

$$\rho_{\lambda} = of f_{\rho} + gain_{\rho} \cdot DN$$

This radiance/reflectance is the one detected by the sensor, that collects several contributions. In particular, in order to obtain the one proper of the surface, atmospheric correction is required. It removes all the effects due to atmospheric phenomena.

This last passage is fundamental if the acquisition occurs by a sensor mounted on satellites or UAVs or any device far enough from the object: in this thesis work the acquisition has been performed by ground and near the object, so this effect can be considered almost negligible and the calibration is performed directly from DN to reflectance of the framed object.

The considered images have been acquired on the 15th September 2020 in a vineyard in Nizza Monferrato. They all represent branches of a vine with its leaves affected by *Peronospora*. The total number of acquisitions is five and the difference between them consists in the set integration time: it is equal to 30 ms, 40 ms, 50 ms, 60 ms, 70 ms.

The radiometric calibration has been performed using MATLAB R2021a software, exploiting Hyperspectral Toolbox. It is able to manage the particular format in which images have been acquired, DAT format.

The images are read and stored in a hypercube, which represents a datacube where the spatial information is represented by x and y coordinates, while spectral information is along z -axis.

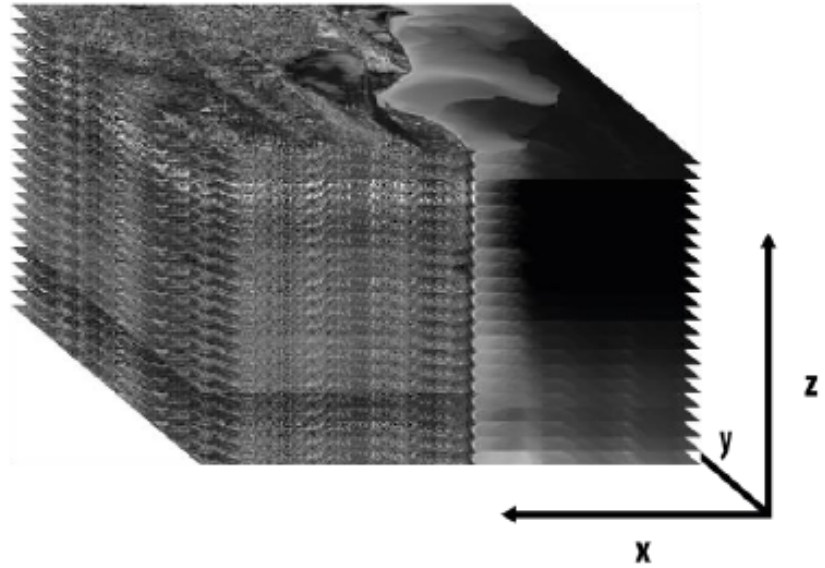


Figure 4.3: *Hypercube: x and y are spatial coordinates, while z is the spectral dimension.* [16]

The aim is to convert this hypercube that contains Digital Numbers associated with each pixel into another one containing instead reflectance values by using the Linear Regression Method. A linear relation between two datasets is found, which means achieving offset and gain of the equation shown above. These two sets are referred to specific target areas of the scene: then the found equation is applied also to all other pixels of the image.

The followed steps for each image are [40]:

- measurement of reflectances and DNs in the same regions corresponding to the calibration target
- modeling the relation between DNs and reflectances just found
- calibration with the confirmed equations

4.2.1 Datasets identification

First of all, reference values collected a priori are necessary, in this case, they represent reference reflectances of the Mapir panel associated with its four regions, black, dark grey, light grey and white. These reflectances are provided in specific files for each band. The spectral behavior is plotted in the following figure.

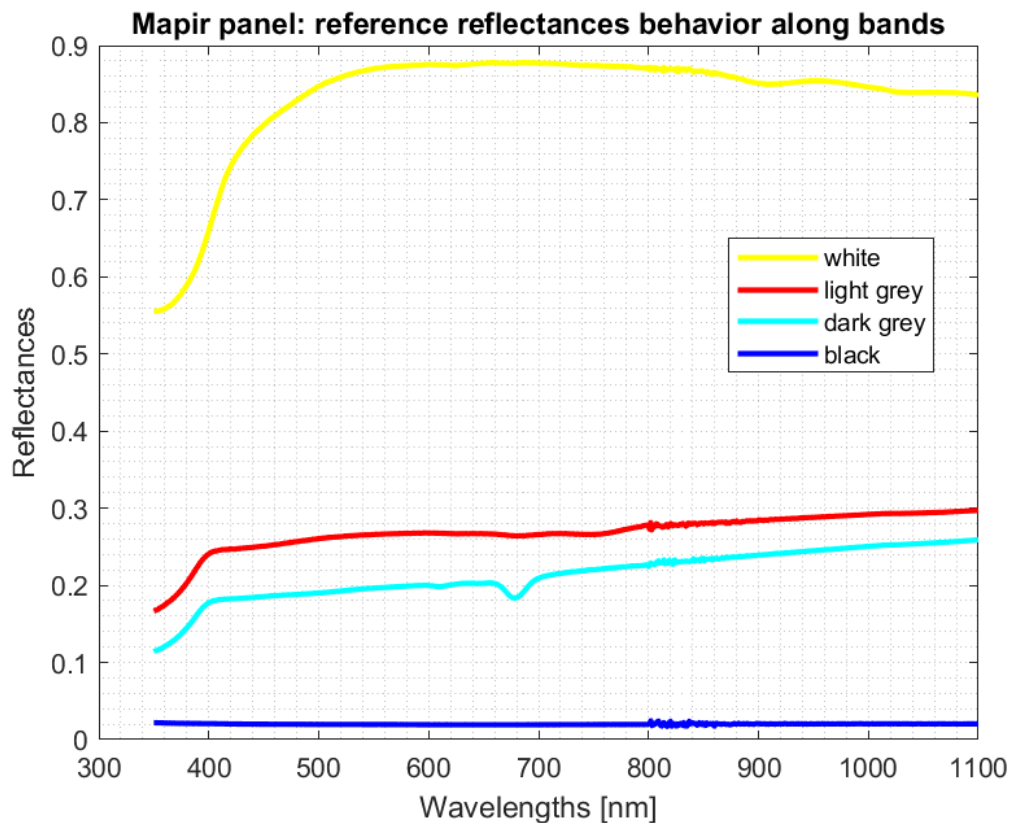


Figure 4.4: *Spectral signature of the four Mapir target regions, therefore behavior of reference reflectances of Mapir panel in function of wavelength. The yellow curve is associated with the white region, the red one to the lighter grey, the light blue is related to the dark grey and the blue line to the black area.*

The white area, associated with the yellow color, presents the highest value of reflectance since almost all the incident radiation is reflected. On the contrary, the black region absorbs the greatest part of the incident rays.

The section of interest is in the range [505.84, 902.39] nm, range proper of the Hyperspectral Rikola camera. This set of data is the same for each image.

The second set of data depends on the image and is represented by Digital Numbers. In order to achieve them, a sequence of steps is necessary for each image. In this report, the procedure is illustrated for the acquisition 'Peronospora_2.bsq', performed with an integration time of 40 ms, but it is equal for all the other images.

The initial process consists in identifying four ROIs (Region of Interest), corresponding to Mapir regions: a region of interest is a group of pixels identified for a specific purpose. Thanks to specific Matlab functions, four rectangles are drawn in correspondence of these areas, avoiding including pixels near the boundaries that could false the information.

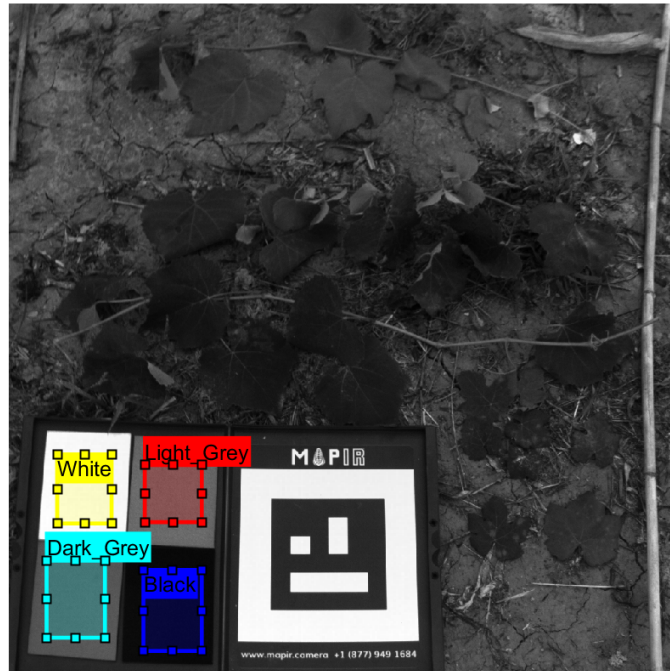


Figure 4.5: ROIs selected in the image acquired with an integration time equal to 40 ms. The color code is the same described before.

Therefore, the polygons' vertices are used to access the hypercube in these regions and extract DN values: all the DNs belonging to each of them are averaged. This is made for each band so that the behavior of averaged DNs can be observed varying the wavelength.

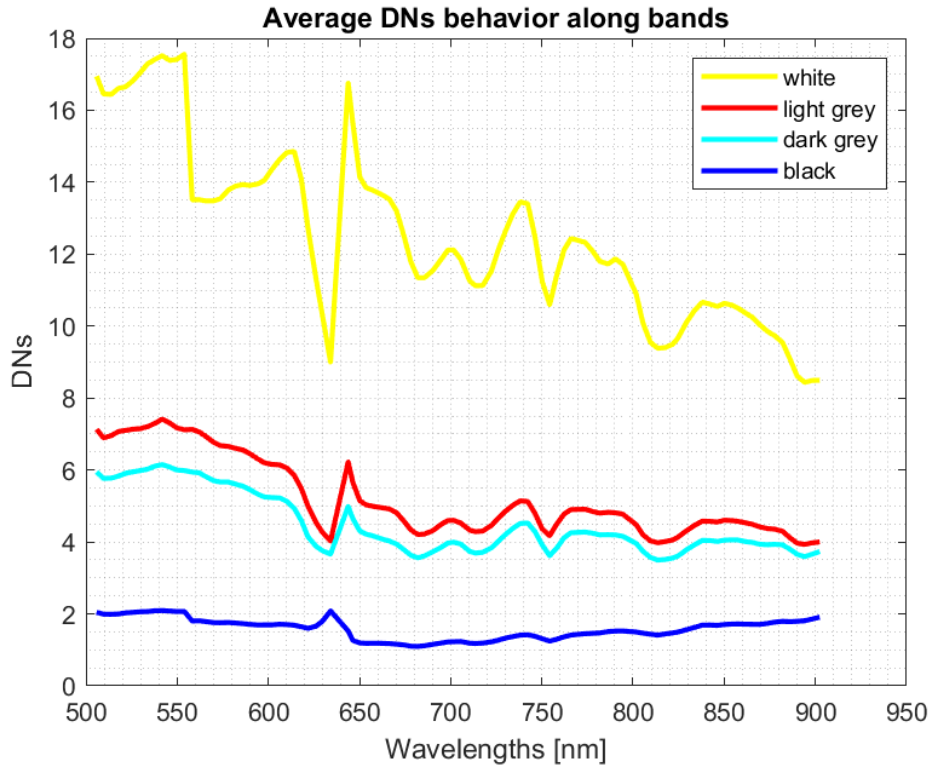


Figure 4.6: *DNs behavior versus wavelength: the average digital numbers for each region is plotted for each band. The curves are irregular.*

As visible, the information does not correspond to the Mapir reflectances in Figure 4.4, the behavior appears more irregular. This shows that DNs are not a true representation of the surface reflectance [39]. They are unreliable data, associated with several additional phenomena, which must be calibrated to maintain a spectral consistency since spectral signature covers a fundamental role in objects characterization.

4.2.2 Calibration relation definition

Now that the two groups of data are available, the LRM can be applied. In particular, for each band, four couples reference reflectance - DN (one for each Mapir target region) are calculated and then interpolation coefficients (gain and offset) are found. The plot appears as follows.

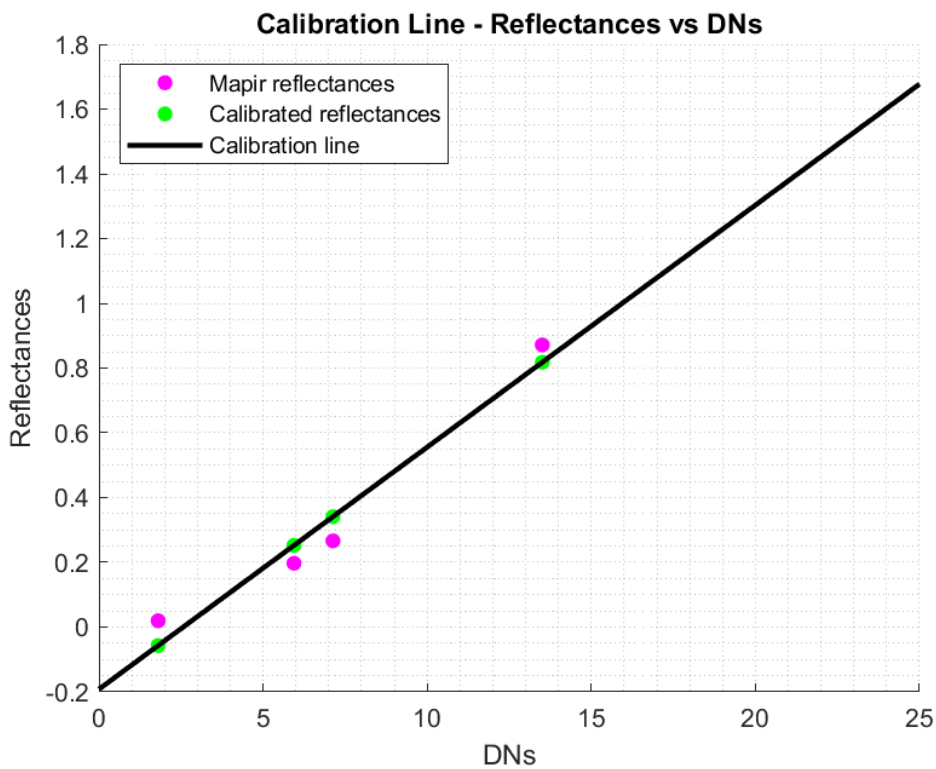


Figure 4.7: Calibration line in band 14. Violet points are the four couples, while green ones are the corresponding values belonging to the line. They can be seen clearly as distinct.

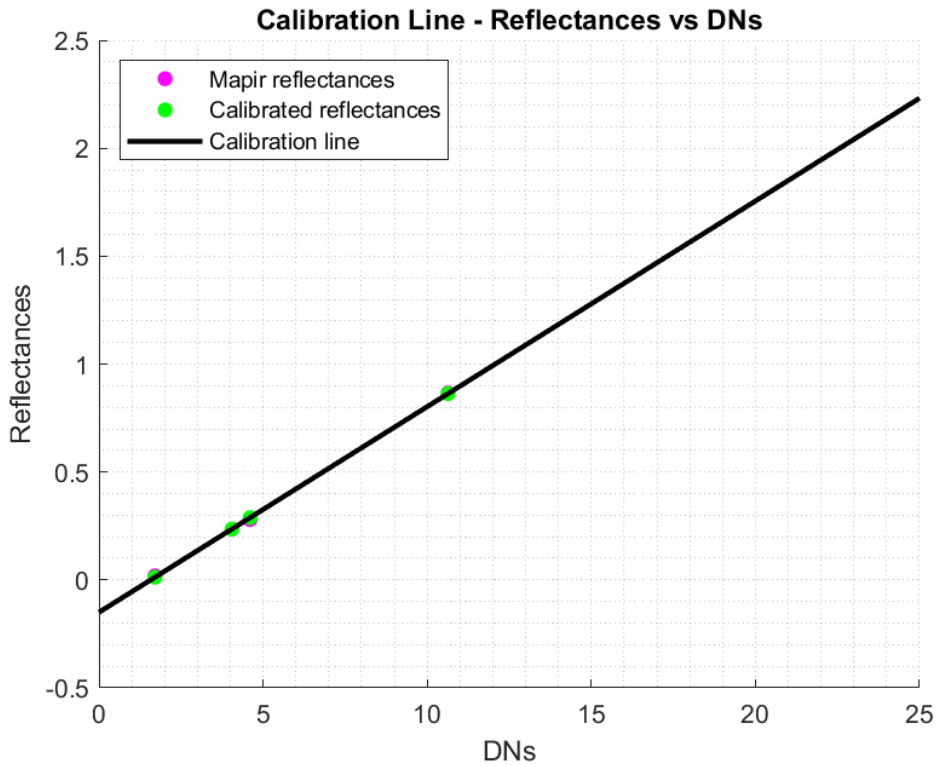


Figure 4.8: *Calibration line in band 84. Violet points are the four couples, while green ones are the corresponding values belonging to the line. In this case they coincide.*

As visible, the y -axis reports reflectances values and the x -axis average DN values. The straight line is the interpolation between the four points (in violet) associated with the four regions of the Mapir panel.

The calibration is optimal starting from about the 30th band, which corresponds to 621.78 nm: they present a similar behavior to Figure 4.4. On the contrary, reference points and predicted ones do not coincide in the lower band range: the worst case is represented by the Figure 4.7 reported above.

In order to verify quantitatively the quality of interpolation, some parameters are computed.

The Root Mean Square Error (RMSE) is a measurement of the difference between the values predicted by the model and the observed points.

$$RMSE = \sqrt{\frac{\sum_{i=1}^4 (\hat{x}_i - x_i)^2}{4}}$$

where x_i represents one of the reflectance values belonging to the reference set, \hat{x}_i is the reflectance value obtained after the calibration. The sum is performed between all the 4 values associated with the four target regions of the Mapir and then they are averaged.

The determination coefficient R^2 is an indicator of the relation between data variability and the correctness of the employed statistical model. It is defined as:

$$R^2 = \frac{ESS}{TSS}$$

where ESS is the Explained Sum of Squares, which represents the sum of the squared deviations of the values estimated by the model from the mean of the real values:

$$ESS = \sum_{i=1}^4 (\hat{x}_i - \bar{x})^2$$

TSS is the Total Sum of Squares, which represents the sum of the squared deviations of the reference values from their mean.

$$TSS = \sum_{i=1}^4 (x_i - \bar{x})^2$$

The obtained values of these two quantities are plotted against the different bands and the following graph is reported.

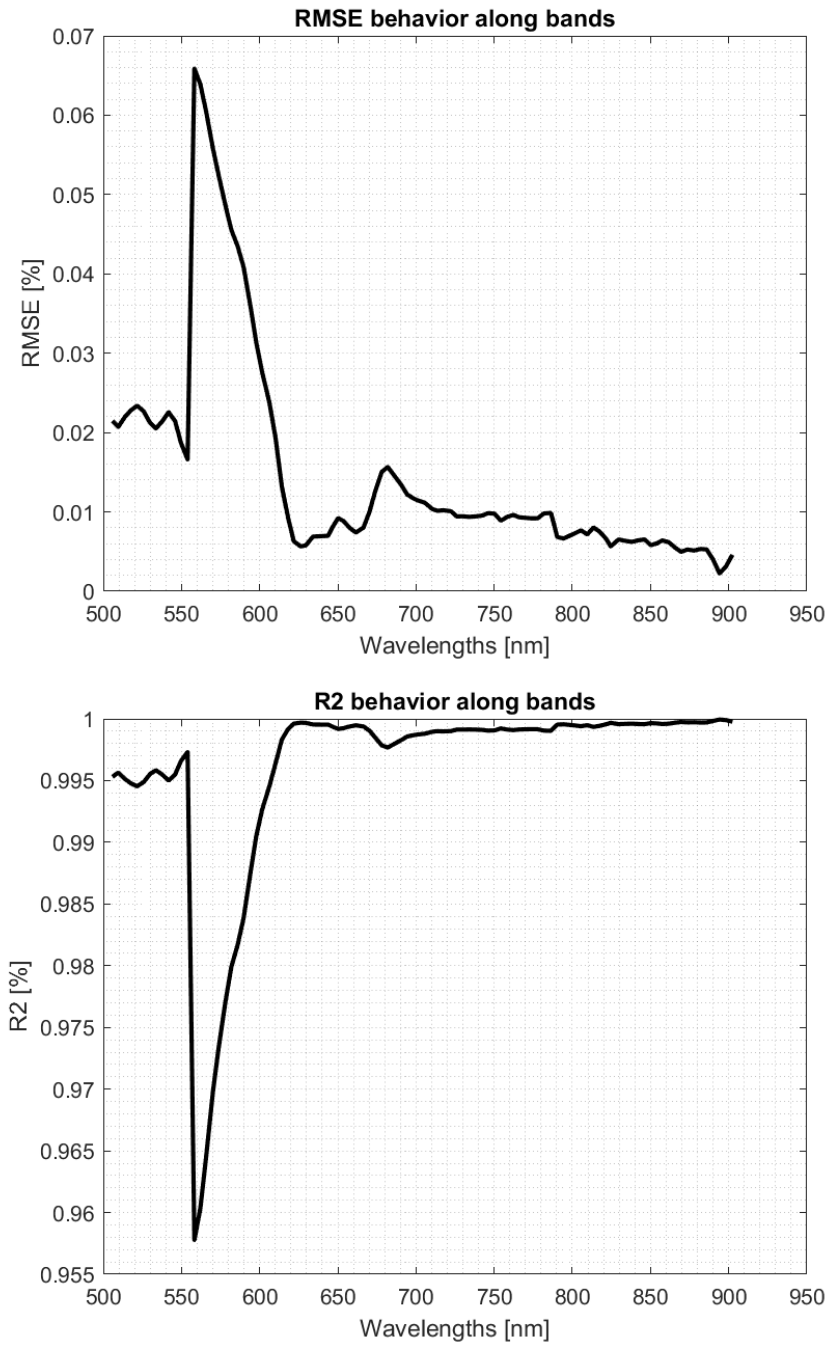


Figure 4.9: On the top RMSE representation, on the bottom R^2 both in function of wavelength. The behavior is uniform and presents optimum values except for the range [550 - 621]nm.

As it has been already noticed observing calibration lines, the bands below about 621 nm do not present an excellent behavior. Indeed, in both RMSE and R^2 graphs there is a peak in correspondence of this interval: in the case of RMSE, it can reach almost 0.07, while all the other values are below 0.01. Considering instead R^2 , in the other bands it is very close to 1, but the glitch falls until about 0.957.

4.2.3 Calibration

Once the calibration line is found for each band, the last step is to convert the DNs contained in the hypercube in reflectances, applying the linear equations just achieved to all the image pixels. An empirical method is used to perform this operation.

In order to verify the correctness of the obtained results, the reflectances values corresponding to the four ROIs are averaged for each region and each band. Similarly to what has been performed before relatively to Digital Numbers, the behavior of reflectances in these target areas is represented in function of wavelength.

Figure 4.10 shows the obtained results.

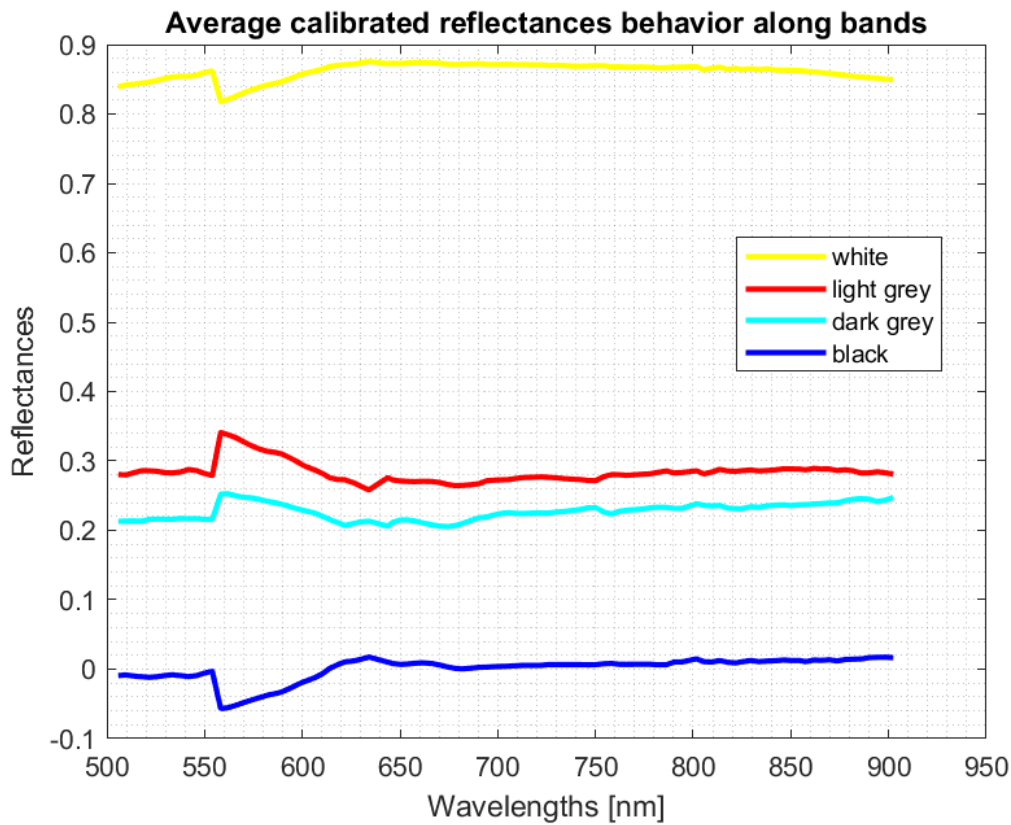


Figure 4.10: *Calibrated reflectance values versus wavelength: for each band, average reflectance calculated with the LRM method is found in each target region. This behavior corresponds to the reference one.*

The figure shows how these curves are more similar, with respect to the DNs curves, to the ones obtained with reference reflectances of the Mapir. The calibration restored the real values of surface reflected radiation excluding the external factors that could influence the measurement. In particular, at high wavelengths the calibration worked more effectively, while at lower ones some deformation in the curves is present. It confirms the behavior already commented in the previous section analyzing statistic parameters for the calibration.

The new hypercube has been converted in a BSQ format in order to obtain an image that can be elaborated.

4.3 Comparison among images results

In the previous sections, only the behavior of the image 'Peronospora_2.bsq', acquired with an integration time of 40 ms, has been analyzed. In the following part, general results from the analysis of the other acquisitions are reported.

In particular, statistical parameters of calibration are elaborated to perform a comparison between all the images.

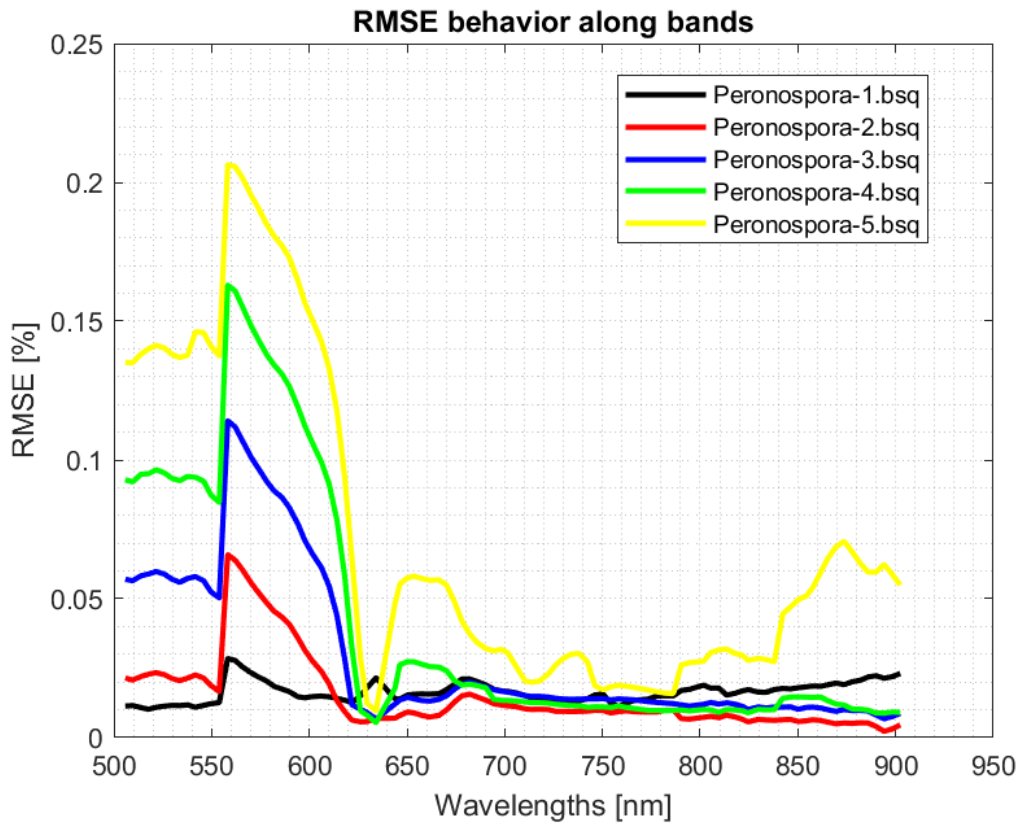


Figure 4.11: *RMSE for each image: the behavior is the same for each image but RMSE gets worse values as integration time increases.*

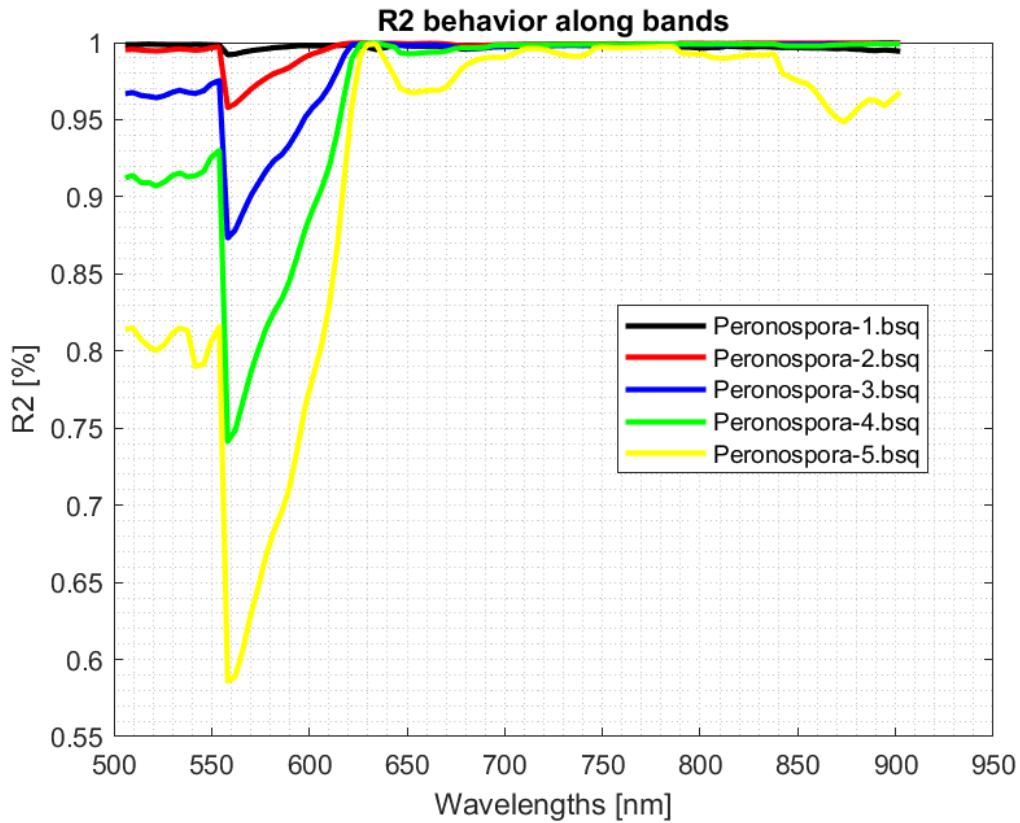


Figure 4.12: R^2 for each image: the behavior is the same for each image but R^2 gets worse values as integration time increases.

As visible from the reported plots, all the images show similar behaviors. A uniform trend can be identified in the bands from about 621 nm, while for lower wavelengths a distinct peak is present: it is related to a worsening of performances for both RMSE and R^2 . This feature is more accentuated as the integration time increases: the yellow curve, corresponding to the image acquired with 70 ms, is the worst case among all the performed acquisitions. On the contrary, the black line is related to an integration time equal to 30 ms and is almost constant.

As a consequence, this behavior is encountered in spectral signatures obtained after calibration.

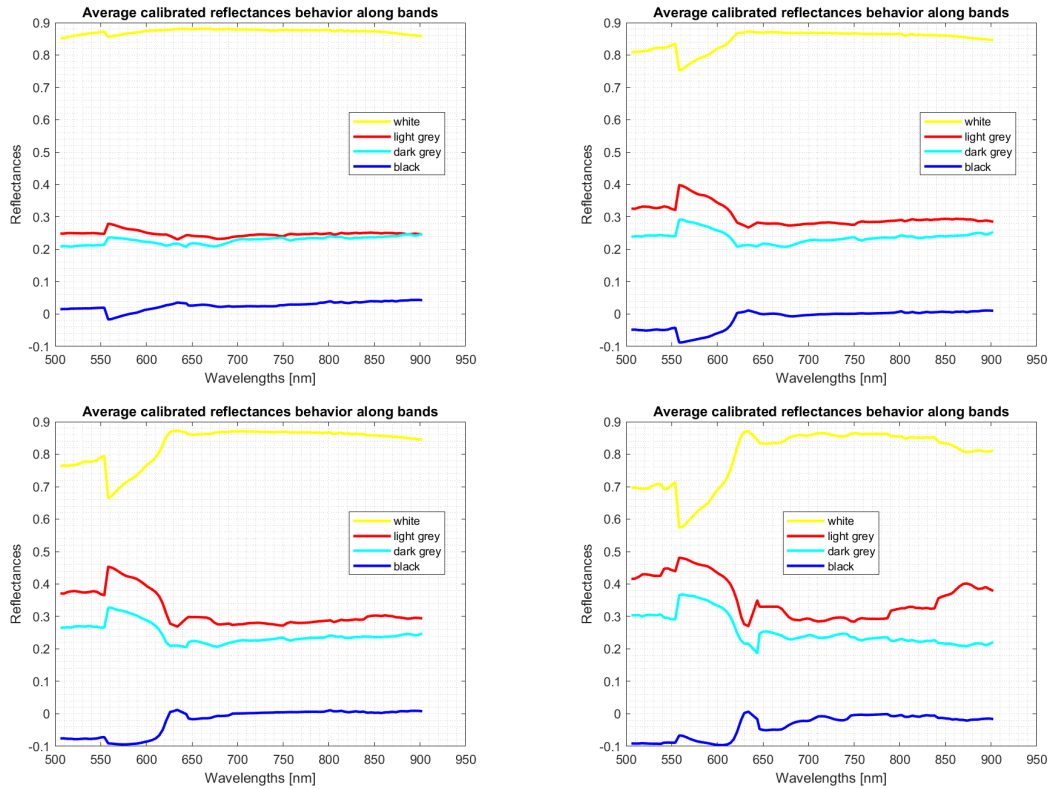


Figure 4.13: *Calibrated reflectances behavior along wavelengths: the top left figure is referred to the image 'Peronospora_1.bsq', acquired with an integration time equal to 30 ms; the top right plot is related to 'Peronospora_3.bsq' (integration time of 50 ms); the bottom left figure has been obtained for 'Peronospora_4.bsq' (integration time of 60 ms); the bottom right corresponds to the image 'Peronospora_5.bsq', acquired with an integration time of 70 ms.*

The obtained graphs are coherent with the statistical analysis performed before on calibration performances.

Chapter 5

Classification

Machine learning is an application of artificial intelligence that concerns the study of systems able to learn automatically from past experiences without being explicitly programmed to do this [17]. They build models starting from sample data, called training data, and then make predictions and take decisions based on them. They can enhance automatically thanks to the experience and large sets of data.

A general scheme that explains the basic functioning of a machine learning algorithm is represented in the following figure.

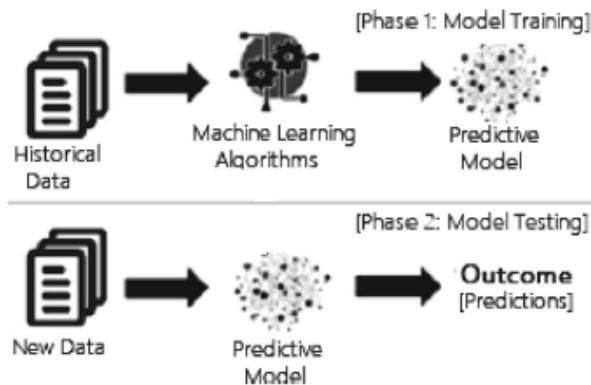


Figure 5.1: *Machine learning scheme: the initial step consists in training the algorithm with specific input data and leads to build a predictive model. Then, this model can be exploited to predict the new data given to the machine [17].*

Depending on the task that must be performed, a different machine learning approach can be selected. They are categorized into four types:

- Supervised learning: the machine is driven to learn a function that maps an input to an output based on input-output pairs [17]. It is trained on a labeled input dataset, which means that input data are associated with a certain label and are provided to the machine. It correlates the features and builds a model based on the labels [41].
- Unsupervised learning: the system attempts to uncover patterns from data [41]. No labels are provided associated with the input data, therefore the model is built starting only from data features, following an iterative process.
- Semi-supervised learning: it is a hybridization of the two described methods since the machine works on both labeled and unlabeled data [17].
- Reinforcement learning: the algorithm is able to take a sequence of decisions in a complex environment, in order to evaluate the optimal behavior in the specified context. It is based on reward and penalty concepts and intends to increase the former and reduce the latter [17].

This study focuses the attention on classification problems, typically relying on supervised learning techniques. It consists in assigning an input to a category, exploiting a classification model defined through automatic learning.

5.1 Procedure

The acquired images, after the radiometric calibration, present a spectral signature that is more reliable and representative of the object characteristics if compared to the curve measured on the original images. Therefore they can be subjected to classification processes, whose goal is to get a thematic map of the image: each pixel is associated with additional information, related to the class to which it belongs [42], relying on its spectral signature. In this specific case, a classifier able to identify *Peronospora* spots on vine leaves can be obtained; several applications in precision agriculture could exploit it to avoid dispersion of curative products against this

disease over large areas where they are not needed.

The operation has been performed with the software ArcGIS Pro and several steps are needed for complete analysis:

- training and classification
- accuracy analysis

The hyperspectral image considered in this study is the one acquired with an integration time of 40 ms, 'Peronospora_2.bsq'. It presents the best spectral signatures between the available acquisitions. Indeed they are more consistent with the spectral curves of the reference reflectances directly measured for the Mapir panel.

5.1.1 Training and Classification

The training phase is a preliminary step necessary for the classifier to learn starting from a training set of measurements representative of the data [43]. First of all, a classification schema must be provided in order to define the different categories present in the image. The decided classes and colors associated with them are shown in the following table.

Class	Color	Identifier
Sane leaves	Green	C_10
Peronospora	Yellow	C_20
Barren	Brown	C_30
Branches	Orange	C_40
White Mapir	Light blue	C_50
Light grey Mapir	Blue	C_60
Dark grey Mapir	Magent	C_70
Black Mapir	Violet	C_80

Table 5.1: *Classes color code: this table indicates the classes selected in this study, the color code associated to them and the identifier used in ArcGIS Pro.*

After that, the definition of the training set is performed. For each class, several polygons are drawn to include the points that will be used in the training process. The selected shapes are visible below.

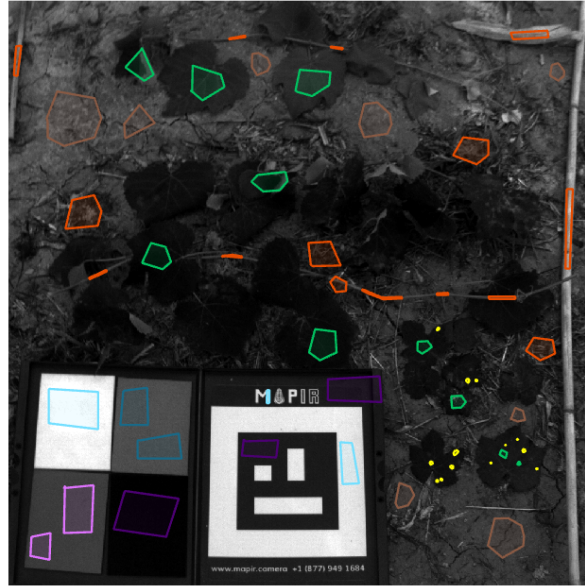


Figure 5.2: *Training ROIs: several shapes are created for each class. The machine builds a model based on these indications, taking into account the spectral signature of the involved pixels.*

It is necessary to decide several aspects that define the classification process. First of all the approach can be pixel-based or object-based: the former performs the classification pixel by pixel ignoring neighbouring pixels values, which are not considered when a class must be assigned. Indeed the spectral content of the pixel determines the class exclusively. The latter groups pixels based on their similarity, in terms of colors and shape, and uses these identified objects to classify the image [44]. The selected procedure, in this case, is the pixel-based one since there are not objects with a distinct and specific shape.

After that, the classification method must be chosen: several machine learning algorithms can be employed, but for this study Support Vector Machine (SVM) and Random Trees (RT) are available.

Support Vector Machine has the purpose of finding hyperplanes in an N-dimensional space that subdivide the different classes in the optimal way. In order to explain in detail the basic principles, a binary problem is illustrated, which refers to a simple case where the distinction between only two classes is required. Therefore, two datasets are present: many possible hyperplanes exist that can separate the two datasets, but the purpose is to define the one that maximizes the distance from the nearest points of each class [45]. Support vectors are the closest points to the hyperplane that influence the position and orientation of the plane: the greater the margin, the lower the classification error [17]. Hence the future data classification becomes more confident and robust.

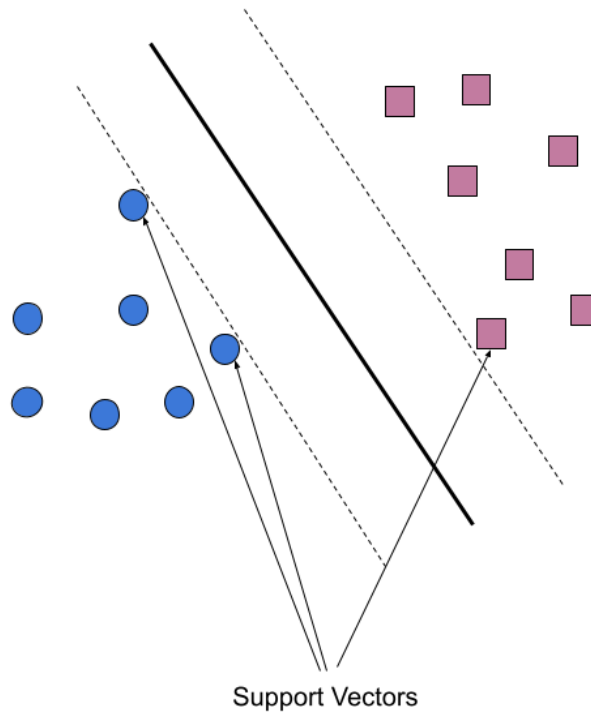


Figure 5.3: *SVM binary classes problem representation: an hyperplane divides the two datasets with the maximum margin from the support vectors. There are many other possible solutions to separate the two groups, but they are not optimal since they do not minimize errors.*

The other implemented algorithm is Random Forest, which consists in the construction of several decision trees [46]. Each tree takes many decisions on a group of data, selected from the training sets, and works independently from the others. The total dataset is classified a number of times that depends on a random subselection of training pixels [44]. The most frequent trees' output becomes the result of the classification. The method allows to avoid the overfitting problem which can occur with a single decision tree; uncorrelated structures can produce ensemble predictions that are more accurate than any of the individual ones[46].

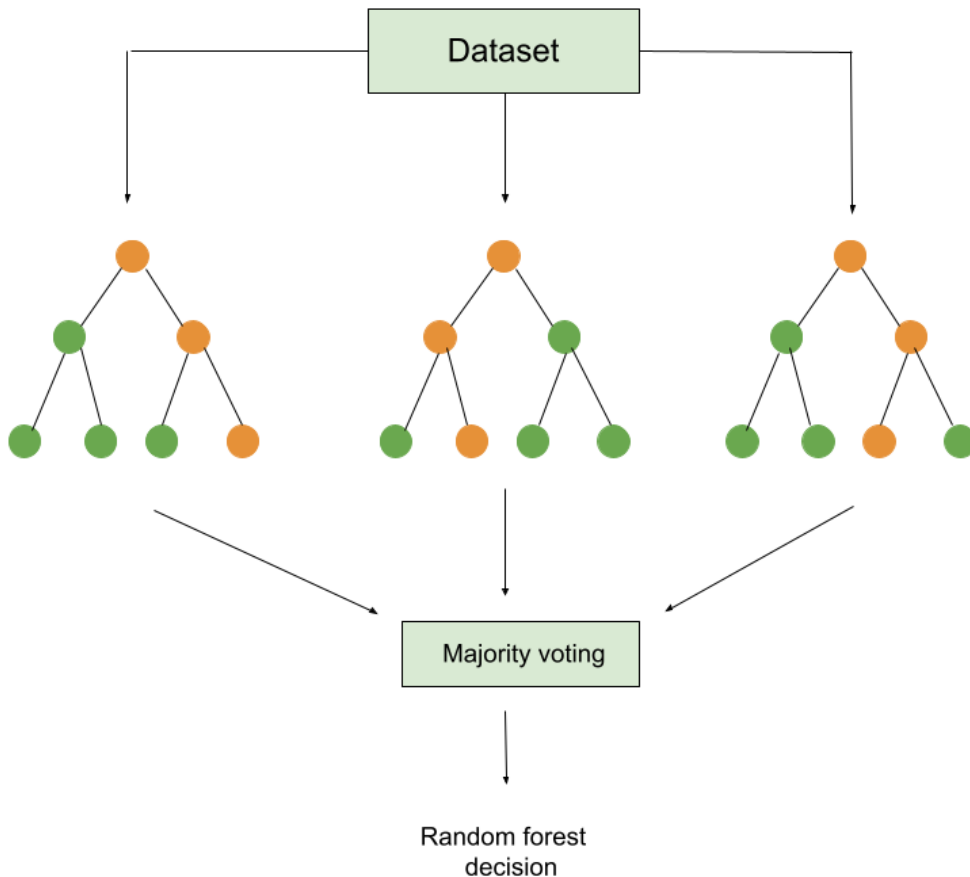


Figure 5.4: *RF representation: several subsets of training data are extracted and associated to a different decision tree. Each of them takes decisions and the final result is defined based on a major voting method, so considering the most frequent outcome of each tree.*

In order to apply the explained methods, it is necessary to set some parameters to define their way of working. In particular, for the SVM algorithm the maximum number of samples to use for defining each class has to be decided. Regarding instead RT case, it is characterized by the maximum number of trees and the maximum depth of each tree, in addition to the maximum number of samples used for each class. The initial configuration is the standard case, suggested to reach a reasonable accuracy.

SVM		RF	
Max samples number	500	Max samples number	1000
		Max trees number	50
		Max tree depth	30

Table 5.2: *First group of settings selected to perform classification.*

The resulting classified images are reported below, considering therefore a pixel based methodology and both SVM and RT algorithms.

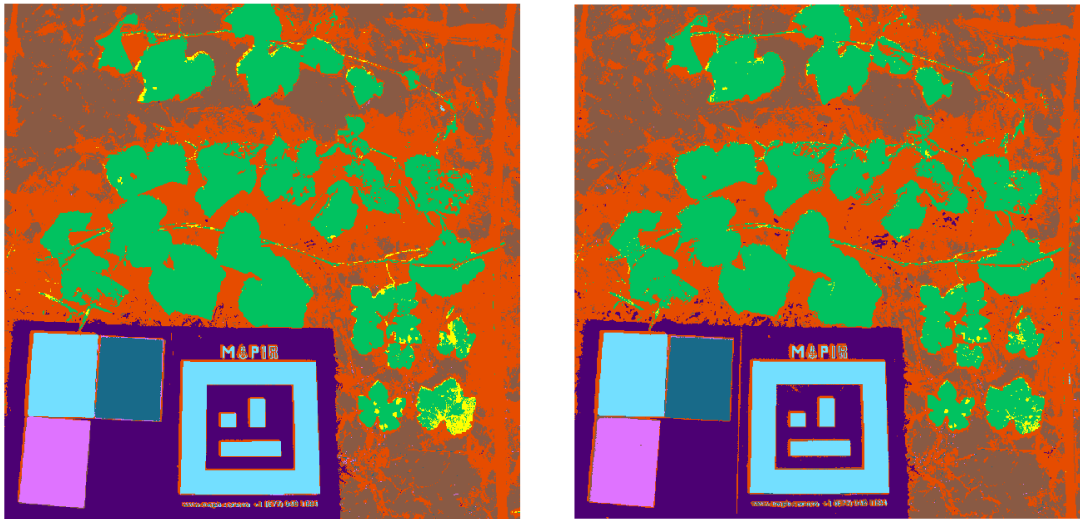


Figure 5.5: *Classified image 'Peronospora_2.bsq': on the left the result of classification performed with the SVM-500 algorithm is shown; on the right the outcome obtained through the RT-30,50,1000 method is visible. Color code is coherent with the Table 5.1*

The obtained classification is comparable for both the tested cases. No great differences can be noticed between the two options. As visible, *Peronospora* spots are clearly identified, in particular on leaves on the right bottom of the image. SVM algorithm highlights a larger region affected by the disease, while RT is able to detect spots in a slightly more precise way. Regarding vine branches, they are not perfectly classified, in particular the ones attached to the leaves.

The two methods differ in terms of velocity of execution: RF is definitely faster than SVM.

Further analysis can be performed considering other values for the setting parameters, in order to control if it is possible to achieve higher accuracy in the classification process. Indeed, a greater number of samples per class takes into account more samples to determine the pixel category and could consider a major variety of conditions. Regarding RT, the precision can be improved also increasing the number of trees in the forest. The new set parameters are the following reported in the table.

SVM		RF	
Max samples number	0	Max samples number	0
		Max trees number	500
		Max tree depth	30

Table 5.3: *Second group of settings selected to perform classification.*

If the maximum number of samples is indicated as 0 in ArcGIS Pro, the program considers all the samples of the described set to train the classifier.

The obtained images are reported in the Figure 5.6.

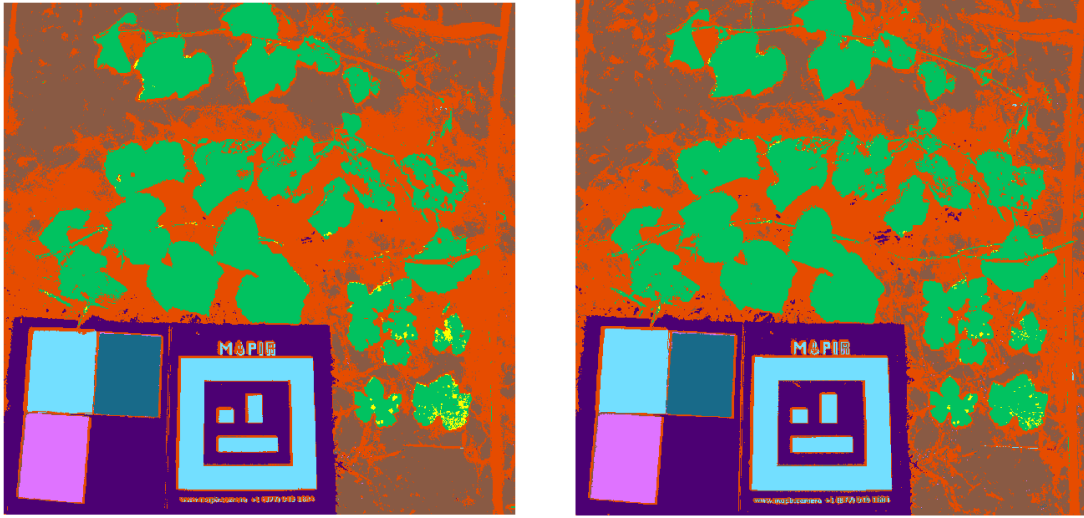


Figure 5.6: *Classified image 'Peronospora_2.bsq': on the left SVM-0 classified outcome is reported; on the right the image elaborated with the RT-30,500,0 algorithm is shown.*

Graphically the obtained classification appears slightly more precise and accurate with respect to the previous case. In particular, observing the Peronospora class, it is less spread and spots are better identified, in particular in SVM tested using all the samples belonging to the ROIs. Moreover, branches attached to leaves are classified correctly if compared to the standard case.

In these examples, the time of execution is strongly increased, in particular considering the SVM algorithm.

5.1.2 Accuracy estimation

The accuracy has been estimated only by observing the obtained classified images so far, but there are methods to achieve a quantitative measurement of this parameter. The confusion matrix is a system that accomplishes this goal. It is an $N \times N$ matrix, where N is the number of defined classes: each column represents the real class to which the pixel belongs (reference or ground truth), while each row corresponds to the class predicted through the classification process [47]. Therefore it contains a diagonal with the number of correctly classified points with respect to their reference values, on the contrary, in the other cells, there are all misclassified points.

An example with only two classes is represented below.

	Actual positive	Actual negative
Predicted positive	true positives	false positives
Predicted negative	false negatives	true negatives

Figure 5.7: *Confusion matrix in case of two classes: the true values represent the points correctly classified, while false ones are associated to classification errors.*

True positives and negatives are the correct predictions, while false negatives and positives represent the points that are not classified correctly and produce wrong predictions.

The sum of rows for each column gives the number of points that have been selected for the specific column class according to the reference data, while the sum of columns for each row is the totality of points classified in the class specified by the row.

In order to compute the confusion matrix, a set of accuracy assessment points is created: they belong to specific ROIs drawn for each class. In particular, it is necessary to define the number of points to generate and the sampling strategy to follow. In this case, the Equalized Stratified Random method creates points randomly distributed within each ROI and each class has the same number of samples [44].

Several sets of ROIs are employed to derive the matrix: in this study, two cases are taken into account, the training set and the verification set. The former exploits the points coming from the set employed for training the classifier, while the latter includes the samples belonging to other ROIs used for verification purposes.

Better accuracy should arise for the training points with respect to the verification ones since the training exploits those ROIs.

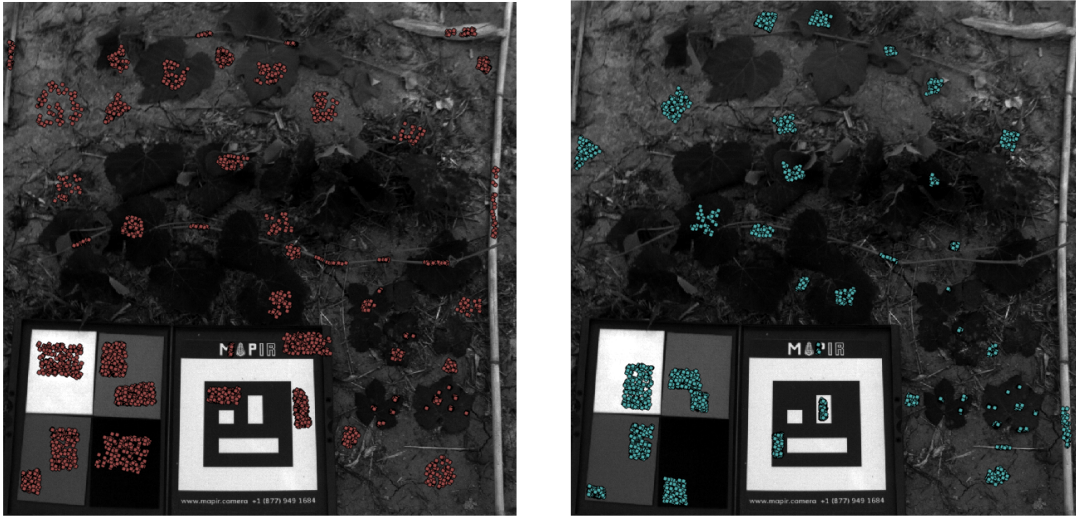


Figure 5.8: *Accuracy points: 500 points are selected from two groups of ROIs, one used for training and the other for verification.*

The quality of classification is measured through several parameters [48]:

- **Producer's Accuracy:** it is calculated for each category as the number of pixels correctly assigned to this class divided by the number of points of the considered class selected to define the confusion matrix. This last parameter includes both correctly classified pixels and the ones that belong to this but are classified in other categories. Referring to the Figure 5.7, which can be extended to multiclass classification, it is computed as follows for the class 'positive':

$$PA = \frac{\#true_positives}{\#true_positives + \#false_negatives}$$

The producer's accuracy is related to the error of omission, which refers to the fraction of pixels belonging to the class that is left out from this category in the map. The lower is this parameter, the higher is the producer's accuracy [49].

- User’s Accuracy: it is computed for each category as the number of pixels correctly classified in this class divided by the total number of pixels classified in the considered class. This last parameter includes both correctly classified pixels and the ones that have been classified wrongly in this category. Referring to the Figure 5.7, for the class ‘positive’:

$$UA = \frac{\#true_positives}{\#true_positives+\#false_positives}$$

The user’s accuracy is related to the error of commission, which refers to the fraction of pixels that is added to this class in the map. The lower is this parameter, the higher is the user’s accuracy [49].

- Kappa coefficient: it measures the general agreement between the actual and classified values.

These quantities are between 0 and 1: the higher the accuracy is, the more exact the classification process appears, respecting actual characteristics.

The confusion matrix for the SVM method with the maximum number of points per class equal to 0 is reported below. It is the algorithm that leads to the best result.

ClassValue	C_10	C_20	C_30	C_40	C_50	C_60	C_70	C_80	Total	U_Accuracy	Kappa
C_10	500	3	0	19	0	0	0	0	522	0,96	0
C_20	0	495	0	0	0	0	0	0	495	1	0
C_30	0	0	499	29	0	0	0	0	528	0,95	0
C_40	0	2	1	452	5	0	0	0	460	0,98	0
C_50	0	0	0	0	495	0	0	0	495	1	0
C_60	0	0	0	0	0	500	0	0	500	1	0
C_70	0	0	0	0	0	0	500	0	500	1	0
C_80	0	0	0	0	0	0	0	500	500	1	0
Total	500	500	500	500	500	500	500	500	4000	0	0
P_Accuracy	1	0,99	1	0,9	0,99	1	1	1	0	0,99	0
Kappa	0	0	0	0	0	0	0	0	0	0	0,98

Figure 5.9: *Confusion matrix ‘Peronospora_2.bsq’*: on the diagonal the correctly classified points are indicated. The other cells contain the number of misclassified samples.

For sake of simplicity, only accuracy measurements are indicated for the other methods: in particular, user’s and producer’s accuracy are indicated only for the *Peronospora* class, which is the focus of this analysis.

SVM-500 training

Kappa	0.97
User’s Accuracy	0.99
Producer’s Accuracy	1

SVM-500 verification

Kappa	0.92
User’s Accuracy	0.88
Producer’s Accuracy	0.86

RT-30,50,1000 training

Kappa	0.96
User’s Accuracy	0.96
Producer’s Accuracy	0.99

RT-30,50,1000 verification

Kappa	0.90
User’s Accuracy	0.93
Producer’s Accuracy	0.81

SVM-0 training

Kappa	0.98
User’s Accuracy	1
Producer’s Accuracy	0.99

SVM-0 verification

Kappa	0.92
User’s Accuracy	0.94
Producer’s Accuracy	0.80

RT-30,500,0 training

Kappa	0.96
User’s Accuracy	1
Producer’s Accuracy	0.88

RT-30,500,0 verification

Kappa	0.89
User’s Accuracy	0.99
Producer’s Accuracy	0.7

Table 5.4: *Accuracy measurements: these tables report the accuracy measurements for all the tested cases on image ‘Peronospora_2.bsq’: SVM-500, RT-30,50,1000, SVM-0 and RT-30,500,0. For each of them, training and verification ROIs are employed to estimate the accuracy.*

The tables show that more accurate outcomes are achieved with the training set of points. As expected, the verification set leads to slightly worse performances. Indeed it is more probable that a point used for training the classifier is correctly categorized.

Analyzing the quantities, the Kappa coefficient assumes similar values considering training sets of different methods: they are all around 0.97, with a peak of 0.98 for the SVM-0 case: these performances correspond to high accuracy. Instead, verification accuracy is around 0.91, which is anyway a good result.

Considering the user's accuracy of *Peronospora* class, it is over 0.96, reaching also 1, in the training cases, related to the fact that a little or null portion of points is classified as *Peronospora* but does not belong to this category.

The producer's accuracy appears very high too: except for the RT-30,500,0 method, which presents a slightly worse value, the others have over 0.99 of precision. This means that few points belonging to *Peronospora* are misclassified in other classes. The lightly best outcomes are obtained again for the SVM-0 case that presents the best values.

Regarding verification parameters, they are rather under 0.9. The worst case is RT-30,500,0 where only a fraction, equal to 0.7, of points of *Peronospora* is correctly classified.

In conclusion, the four employed methods do not lead to performances too different, focusing the attention on the *Peronospora* class that is the core of the analysis; small divergencies are visible, which identify the SVM-0 method as the slightly most accurate, but the results are comparable. The increment of maximum samples per class does not influence significantly the classification in this study, meaning that a number of points per class equal to 500 is reasonable to obtain good accuracy. Hence the time of execution of the classification process can be dramatically reduced by exploiting the suggested settings, in particular in the case of the Support Vector Machine algorithm. Regarding Random Forest, neither the maximum number of trees affects in a meaningful way classification performances in this study.

5.2 Porting

After training and classification of the considered image, the obtained classifier can be exploited and used on other acquisitions. This phase is called Porting: in particular, it consists in applying the classification achieved in the previous section on other images in order to classify them without defining ROIs and training the machine. It is a simpler and faster method that is used to understand if the classification appears accurate and reliable.

In this study, the step of Porting is applied to the image 'Peronospora_3.bsq' acquired with an integration time equal to 50 ms, since it presents the most similar calibration curves to the studied one. The obtained classified image is reported below, considering both classification algorithms with all the settings tested and explained in the previous sections.

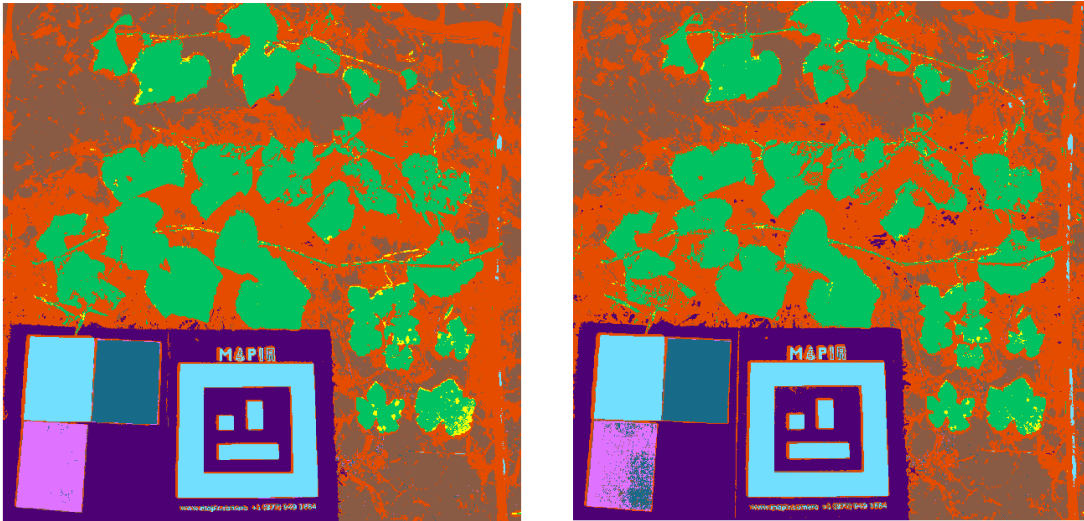


Figure 5.10: *Porting on image 'Peronospora_3.bsq': both SVM and RF algorithms are employed, with the configuration indicated in the Table 5.2*

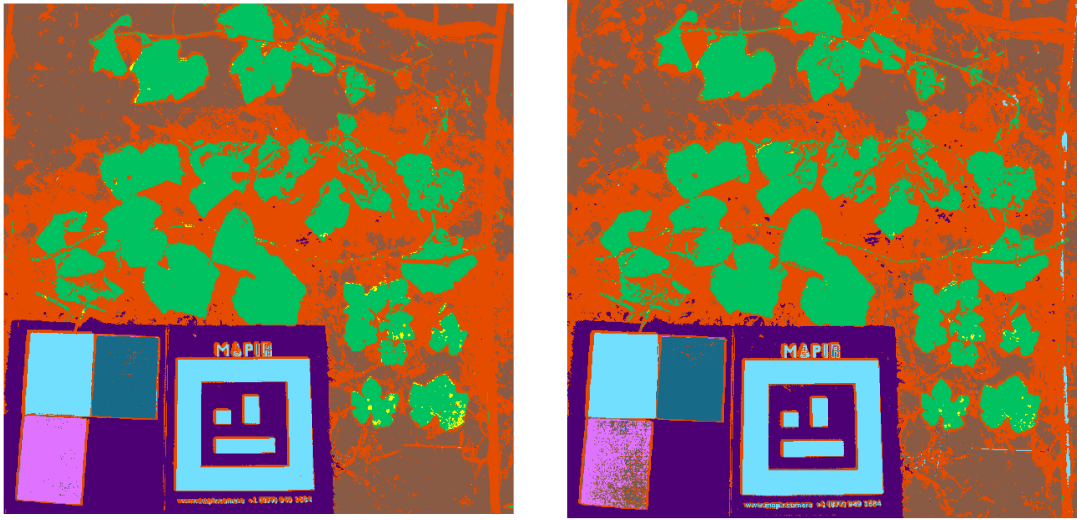


Figure 5.11: *Porting on image 'Peronospora_3.bsq': both SVM and RF algorithms are employed, with the configuration indicated in the Table 5.3*

Observing the images, the method that leads to the best classification is again obtained with SVM-0: a more accurate representation of classes is obtained. The quantitative measurements of accuracy are reported below.

SVM-500		RT-30,50,1000	
Kappa	0.93	Kappa	0.83
User's Accuracy	1	User's Accuracy	1
Producer's Accuracy	0.89	Producer's Accuracy	0.71

SVM-0		RT-30,500,0	
Kappa	0.96	Kappa	0.81
User's Accuracy	1	User's Accuracy	1
Producer's Accuracy	0.85	Producer's Accuracy	0.6

Table 5.5: *Porting accuracy: these tables report the accuracy measurements obtained after the Porting application on the image 'Peronospora_3': the same methods and their configuration tested in the previous section are used, SVM-500, RT-30,50,1000, SVM-0 and RT-30,500,0.*

The measurements confirm the graphical view: SVM-0 performs a more precise classification, while RT-0 is the worst performant method. In this case, a more evident difference is visible between Support Vector Machine and Random Trees algorithms if compared to the case presented in the previous section: in particular, higher accuracy is obtained with the former.

The porting operation leads to reasonable results in this image that presents similar spectral signatures to the ones of the image 'Peronospora_2.bsq', used for training. Moreover, they are the most coherent curves obtained after calibration since they are comparable to the reference ones directly measured on the field. Whenever the considered signatures differ, classification is no more reliable. An example is constituted by the image 'Peronospora_5.bsq', acquired with 70 ms of integration time. Calibration curves are different from the ones of image 'Peronospora_2.bsq' and are less consistent with the reference values. Therefore it is encountered that classifiers trained in previous sections do not fit this case.

The obtained results are not satisfying. The best case between all the tried methods is the SVM-500, which presents a Kappa coefficient equal to 0.7 and user and producer's accuracy equal respectively to 0.8 and 0.5. The other algorithms lead to Kappa coefficients equal to 0.4 and accuracies of 0.2 in the worst case.

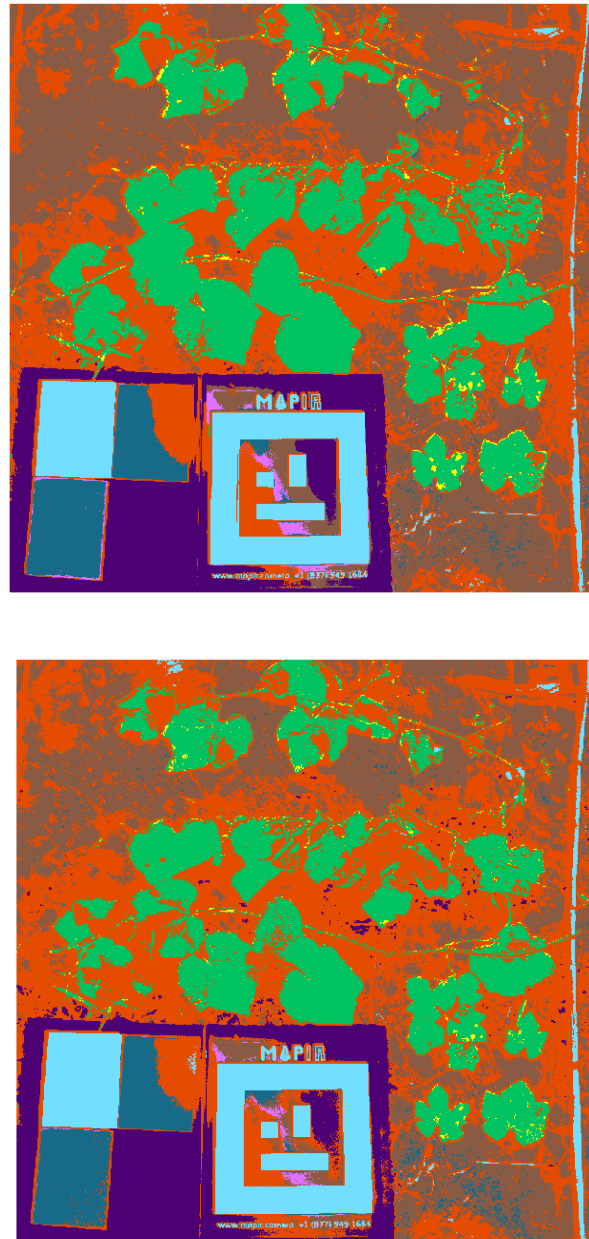


Figure 5.12: *Porting on image 'Peronopora_5.bsq': the image represents the best case, obtained with SVM-500 method. The classification does not respect the real features.*

5.3 Application

The obtained classifier can find several applications: it can be employed to detect *Peronospora* effects in other situations. In particular, in this study, it is applied to an acquisition that represents a vineyard row. The image was already calibrated [42].



Figure 5.13: *Vineyard row represented with Mapir panel*

The four obtained classifiers are applied to this image and the resulting classification appears as reported below. In particular, only one image per algorithm is considered, since different settings produce equal outcomes.

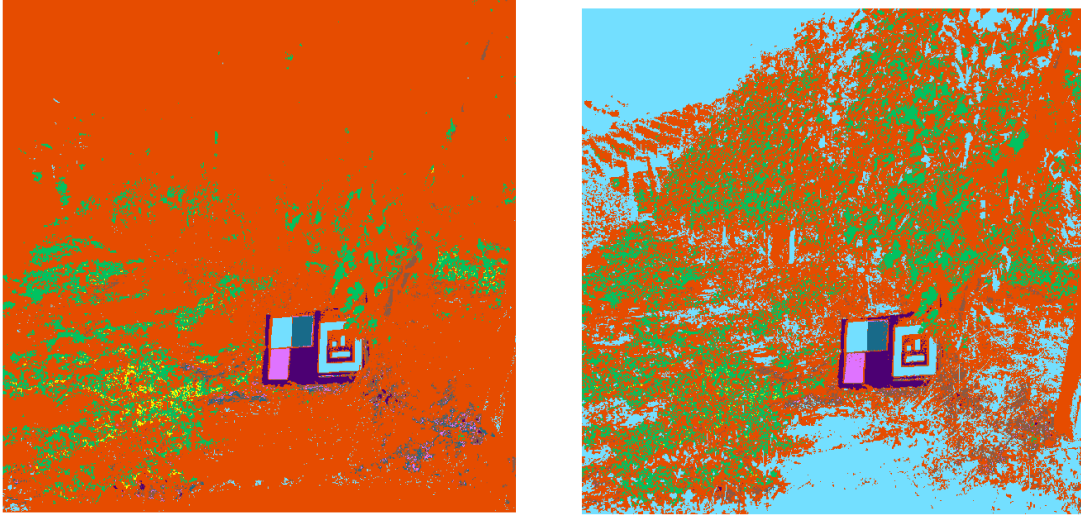


Figure 5.14: *Classification of a vineyard row: the image on the left is the result of the application of the SVM method, while the image on the right reports the classification performed with RT.*

In this case, Support Vector Machine does not lead to a reliable classification: indeed almost the complete figure, except for a few areas, is classified as branches. On the contrary, RT leads to a more reasonable result: it must be noticed that in the image there are elements that belong to classes that are not present in the classifier since the image is different from the one on which training has been performed. Therefore, several areas are not correctly classified: these are mainly the sky, clouds and grapes, which are not present in the elaborated image 'Peronospora_2.bsq'. However, the row is composed of branches and leaves and Peronospora must be searched between the latter. The classifier does not identify any track of the disease, meaning that the present leaves are all sane.

Chapter 6

Conclusions

This thesis work has shown the elaboration steps to perform on hyperspectral images from their acquisition for specific applications in the precision agriculture environment. In particular, the goal was to produce classifiers able to detect Peronospora disease on vine leaves based on the spectral signature of pixels that compose the image.

The images have been calibrated, removing external factors' influence, and then subjected to the classification process. Several machine learning algorithms have been used to train the image 'Peronospora_2.bsq': Support Vector Machine and Random Trees. Their parameters have been tuned to obtain higher accuracy. The slightly best result is represented by the SVM method that employs all the defined points to train the machine; however, the other techniques lead to comparable outcomes.

The achieved classifiers are applied to other images, performing Porting operation: it has been encountered that the more similar the spectral signature obtained after calibration are to the ones of the classified acquisition, the more accurate the classification of the new image is. Indeed, the analysis on 'Peronospora_3.bsq' appears more reasonable with respect to 'Peronospora_5.bsq', which has calibration curves less consistent with the reference ones.

Then a completely different image has been classified: it represents a vineyard row. In this case, RT produced a more reliable result, showing that Peronospora is not present on the leaves present in the image.

Possible future work could concern the use of deep learning techniques to perform the classification and compare the obtained results to the ones achieved with machine learning techniques. Indeed, deep learning is represented by a set of algorithms organized in several layers characterized by neural network-like behavior.

The Rikola camera could be mounted on automatic platforms that move through the vineyard. It may be a part of a system that exploits the operations illustrated in this study to take decisions automatically regarding the use of specific products in precise regions where *Peronospora* is detected.

Bibliography

- [1] GCSE resources for students. *Electromagnetic spectrum and light*. https://erewhon.xyz/resources/categories.php?category_id=70&subject_id=12?subject_name=Physics&subjectName=Physics&categoryGroup=electromagnetic-spectrum-and-light.
- [2] Sentek Systems. *What is remote sensing*. <http://www.senteksystems.com/2015/11/17/what-is-remote-sensing-1/>.
- [3] Adão Telmo, Hruška Jonáš, Pádua Luís, Bessa José, Peres Emanuel, Raul Morais, and Joaquim João Sousa. *Hyperspectral Imaging: A Review on UAV-Based Sensors, Data Processing and Applications for Agriculture and Forestry*. *Remote Sensing*, 9(11):1110, October 2017.
- [4] Saari Heikki. *Properties and calibration of MEMS and piezoactuated Fabry-Perot Spectral Imagers*. In *EUFAR Joint Expert Working Group Meeting: Imaging Spectroscopy Sensor, Calibration/Validation and Data Processing*. VTT Technical Research Centre of Finland, Edinburgh, April 2011.
- [5] Caffi Tito, Rossi Vittorio, Gilardi Giovanna, Monchiero Matteo, Gullino Maria Lodovica, and Spanna Federico. *Studi epidemiologici su Plasmopara viticola*. 2010.
- [6] Istituto agrario. *Peronospora della vite*. <https://www.istitutoagrariosartor.edu.it>, October 2016.
- [7] Mapir. *Mapir Camera Reflectance Calibration Ground Target Package (V2)*. <https://www.mapir.camera/products/mapir-camera-reflectance-calibration-ground-target-package-v2>.

- [8] Cannarozzo, Cucchiarini, and Meschieri. *Capitolo 1 - Principi e strumenti della fotogrammetria*. In *Metodi, Misure, Rilievi*. Zanichelli editore S.p.A., Bologna, 2012.
- [9] MathWorks. *What is camera calibration?* <https://www.mathworks.com/help/vision/ug/camera-calibration.html>.
- [10] Tykkälä Tommi. *Real-time image-based RGB-D camera motion tracking and environment mapping*. PhD thesis, Université Nice Sophia Antipolis, 2013.
- [11] Wang Quanzeng, Cheng Wei-Chung, Suresh Nitin, and Hua Hong. *Development of the local magnification method for quantitative evaluation of endoscope geometric distortion*. *Journal of Biomedical Optics*, 21(5):056003, May 2016.
- [12] Geekering. *Introduction to Computer Vision - Camera Calibration*. <https://www.geekering.com/categories/computer-vision/jaimesilva/introduction-to-computer-vision-camera-calibration/>.
- [13] Drap Pierre and Lefèvre Julien. *An Exact Formula for Calculating Inverse Radial Lens Distortions*. *Sensor*, 16(6):807, June 2016.
- [14] Musci Maria Angela, Aicardi Irene, Dabove Paolo, and Lingua Andrea. *Reliability of the geometric calibration of an hyperspectral frame camera*. *ISPRS - International Archives of the Photogrammetry, Remote Sensing and Spatial Information Sciences*, XLII-2/W13:1701–1707, June 2019.
- [15] Krivanek Jaroslav. *Radiometry*. In *Computer Graphics III*.
- [16] Vaccaro A. *Il telerilevamento iperspettrale: Messa a punto e calibrazione di una camera iperspettrale*. Master’s thesis, Università degli studi di Palermo, 2017.
- [17] Sarker Iqbal H. *Machine learning: Algorithms, real-world applications and research directions*. *SN Computer Science*, 2(3):1–21, 2021.
- [18] Prachi Singh, Prem Chandra Pandey, George P Petropoulos, Andrew Pavlides, Prashant K Srivastava, Nikos Koutsias, Khidir Abdala Kwai Deng, and Yangson Bao. *Hyperspectral remote sensing in precision agriculture: present status,*

- challenges, and future trends.* In *Hyperspectral Remote Sensing: Theory and Applications*, pages 121–146. Elsevier, Amsterdam, 2020.
- [19] Casa R. and Pisante M. *Introduzione.* In *Agricoltura di precisione: Metodi e tecnologie per migliorare l'efficienza e la sostenibilità dei sistemi colturali.* Edagricole-Edizioni Agricole di New Business Media Srl, 2016.
- [20] Castellari S., Venturini S., Giordano F., Ballarin Denti A., Bigano A., Bindi M., Bosello F., Carrera L., Chiriaco M.V., Danovaro R., Desiato F., Filpa A., Fusani S., Gatto M., Gaudio D., Giovanardi O., Giupponi C., Gualdi S., Guzzetti F., Lapi M., Luise A., Marino G., Mysiak J., Montanari A., Pasella D., Pierantonelli L., Ricchiuti A., Rudari R., Sabbioni C., Sciortino M., Sinisi L., Valentini R., Viaroli P., Vurro M., and Zavatarelli M. *Elementi per una Strategia Nazionale di Adattamento ai Cambiamenti Climatici - Introduzione.* Ministero dell' Ambiente e della Tutela del Territorio e del Mare, Roma, 2014.
- [21] Zarco-Tejada Pablo J., Hubbard N., and Loudjani Ph. *Precision agriculture: An opportunity for EU farmers - Potential support with the CAP 2014-2020.* Joint Research Centre (JRC) of the European Commission, 2014.
- [22] Biglia A., Comba L., Gay P., Grella M., and Manzone M. *Agricoltura 4.0: Nuove opportunità tecnologiche tra presente e futuro.* In *Agricoltura 100.* Regione Piemonte, Luglio 2021.
- [23] Sishodia Rajendra P., Ray Ram L., and Singh Sudhir K. *Applications of Remote Sensing in Precision Agriculture: A Review.* *Remote Sensing*, 12(19):3136, September 2020.
- [24] AgroAmbiente.Info. *Peronospora della vite.* <http://agroambiente.info.arsia.toscana.it/arsia/arsia?ae5Diagnosi=si&IDColtura=2&IDSchedaFito=1>.
- [25] USGS science for a changing world. *What is remote sensing and what is it used for?* https://www.usgs.gov/faqs/what-remote-sensing-and-what-it-used?qt-news_science_products=0\protect\char35\relaxqt-news_science_products.

- [26] Morigi M. *Il telerilevamento e i sistemi informativi territoriali per l'analisi dei cambiamenti della linea di costa*. ISPRA.
- [27] Mapware. *A complete guide to remote sensing*. <https://www.mapware.ai/remote-sensing>.
- [28] Sansó F. *Analisi di dati telerilevati ottici e radar per la gestione di disastri: le alluvioni del Bangladesh*. Master's thesis, Università di Bologna, 2011.
- [29] Shunlin Liang and Jindi Wang. *Chapter 1 - A systematic view of remote sensing*. In *Advanced Remote Sensing (Second Edition)*. Academic Press, 2020.
- [30] Satellite Application for Geoscience Education. *Remote Sensing - Spatial Analysis*. https://cimss.ssec.wisc.edu/sage/remote_sensing/lesson3/concepts.html.
- [31] Kokka Alexander, Pulli Tomi, Honkavaara Eija, Markelin Lauri, Kährä Petri, and Ikonen Erkki. *Flat-field calibration method for hyperspectral frame cameras*. *Metrologia*, 56(5):055001, August 2019.
- [32] Utenti.quipo. *Interferometro di Fabry-Perot*. <http://utenti.quipo.it/itislanciano/bande/Interferometro.htm>.
- [33] Rossi Vittorio, Caffi Tito, Giosué Simona, Girometta Benedetta, Bugiani Riccardo, Spanna Federico, Dellavalle Daniele, Brunelli Alessandro, and Collina Marina. *Elaboration and validation of a dynamic model for primary infections of *Plasmopara viticola**. *Rivista Italiana Di Agrometeorologia*, 2, January 2005.
- [34] Melis D. *Un algoritmo per la Camera Calibration basato sulla visione stereoscopica*. Master's thesis, Università degli studi di Cagliari, 2017.
- [35] Hönlinger B. and Nasse H.H. *Distortion*. In *Camera Lens Division*. Carl Zeiss, October 2009.
- [36] Xu Kaiqiu, Gong Yan, Fang Shenghui, Wang Ke, Lin Zhiheng, and Wang Feng. *Radiometric Calibration of UAV Remote Sensing Image with Spectral Angle Constraint*. *Remote Sensing*, 11(11):1291, 2019.

- [37] MathWorks. *Hyperspectral data correction*. <https://de.mathworks.com/help/images/hyperspectral-data-correction.html>.
- [38] Dronebee. *La riflettività ed i sensori multispettrali*. <https://www.dronebee.it/riflettanza/>.
- [39] Iqbal Faheem, Lucieer Arko, and Barry Karen. *Simplified radiometric calibration for UAS-mounted multispectral sensor*. *European Journal of Remote Sensing*, 51(1):301–313, February 2018.
- [40] Guo Yahui, Senthilnath J., Wu Wenxiang, Zhang Xueqin, Zeng Zhaoqi, and Huang Han. *Radiometric Calibration for Multispectral Camera of Different Imaging Conditions Mounted on a UAV Platform*. *Sustainability*, 11(4):978, 2019.
- [41] Towards Data Science. *Machine learning - Fundamentals*. <https://towardsdatascience.com/machine-learning-basics-part-1-a36d38c7916>.
- [42] Parizia F. *Usa di immagini iperspettrali per l'agricoltura di precisione*. Master's thesis, Politecnico di Torino, 2021.
- [43] Zalev Jason and Kolios Michael C. *Detecting abnormal vasculature from photoacoustic signals using wavelet-packet features*. In *Photons Plus Ultrasound: Imaging and Sensing 2011*, volume 7899, page 78992M. International Society for Optics and Photonics, 2011.
- [44] ArcGIS Pro. *The Image Classification Wizard*. <https://pro.arcgis.com/en/pro-app/2.7/help/analysis/image-analyst/the-image-classification-wizard.htm>.
- [45] Maxwell Aaron E., Warner Timothy A., and Fang Fang. *Implementation of machine-learning classification in remote sensing: An applied review*. *International Journal of Remote Sensing*, 39(9):2784–2817, 2018.
- [46] Towards Data Science. *Understanding Random Forest*. <https://towardsdatascience.com/understanding-random-forest-58381e0602d2>.

BIBLIOGRAPHY

- [47] Story Michael and Congalton Russell G. *Accuracy assessment: a user' s perspective*. *Photogrammetric Engineering and remote sensing*, 52(3):397–399, 1986.
- [48] Patel Nilanchal and Kaushal Brijesh Kumar. *Improvement of user' s accuracy through classification of principal component images and stacked temporal images*. *Geo-spatial Information Science*, 13(4):243–248, 2010.
- [49] L3Harris Geospatial. *Calculate Confusion Matrix*. <https://www.l3harrisgeospatial.com/docs/calculatingconfusionmatrices.html>.